ABSTRACT

Preparation of Promising Substrates for Surface-Enhanced Raman Spectroscopy

Bryan Jan

Director: Dr. Zhenrong Zhang, Ph.D

The goal of this study was to fabricate and characterize metal thin films of silver and aluminum to determine the effects of deposition thickness and deposition temperature on nanoparticle morphology and size. Chemical thin films were successfully synthesized by physical vapor deposition (PVD) onto various substrates. Depositions were accomplished by either thermal evaporation or electron beam evaporation. A collimator was implemented that reduced the evaporation spot size of the thermally evaporated copper phthalacyanine (CuPc). Electron beam deposition of silver and aluminum yielded thin films that were confirmed with energy-dispersive X-ray spectrometry and X-ray diffraction. Surface nanostructures were analyzed with scanning electron microscopy (SEM). A trend of increasing density for silver island clusters with increased deposition thickness was noted. Increased nanoparticle size for depositions at elevated temperature was also observed. Similarly, thicker depositions of aluminum yielded larger nanoparticles and a trend of increased nanoparticle size was observed for elevated temperature depositions. Further research to characterize and optimize deposition parameters for surface-enhancement of Raman signals is necessary.

APPROVED BY DIRECTOR OF HONORS THESIS:

_____

Dr. Zhenrong Zhang, Department of Physics

APPROVED BY THE HONORS PROGRAM:

_____

Dr. Andrew Wisely, Director

DATE: _____

PREPARATION OF PROMISING SUBSTRATES FOR SURFACE-ENHANCED RAMAN SPECTROSCOPY

A Thesis Submitted to the Faculty of

Baylor University

In Partial Fulfillment of the Requirements for the

Honors Program

By

Bryan Jan

Waco, Texas

May 2015

TABLE OF CONTENTS

ACKNOWLEDGMENTS

I owe my deepest gratitude to my thesis mentor and committee chair, Dr. Zhenrong Zhang, for unfailingly devoting her time and attention to the completion of this thesis and to my holistic education of research. Her guidance often motivated my work within the lab and gave direction to my writing. I give special thanks to her for allowing me, a Biochemistry and Biology major, to join a Physics research group.

In addition, I offer my deepest gratitude for my committee members, Dr. Kenneth Park and Dr. Kevin Shuford for challenging me to think about topics and questioning my understanding in new and enlightening ways. Their attention helped to further my work to the level at which it is currently.

This thesis would also not have been possible had it not been for the countless hours of focus spent by Dr. Bernd Zechmann. His commitment to attaining the most optimal images on the Center for Microscopy and Imaging's Scanning Electron Microscope can be seen in the quality of the images obtained.

I would like to offer a huge hand of thanks to my colleagues in the research lab. The wealth of knowledge and the introduction to unfamiliar topics provided a stable and firm foundation to my current work.

Finally, I would like to thank Baylor University and the Baylor Department of Physics for funding and allowing my research. Additionally, thanks to the Summer Undergraduate Research in Physics fund that extended my time in lab to outside the confines of the academic year.

To my mother without whom I would not be at college

To my many friends who encouraged and inspired me throughout this process

To the many professors who served as sources of wisdom and inspiration

CHAPTER ONE

Introduction

1.1 Surface Enhanced Raman Spectroscopy

Recent advances in instrumentation and theoretical understanding of surface-enhanced Raman spectroscopy (SERS) have bolstered its establishment as an analytical and spectroscopic tool. The discovery of "scattered light with diminished energy" in 1928 by Raman and Krishnan opened the door to further discoveries of Raman spectroscopy as a means of diagnostic selectivity. [1] Raman spectroscopy specifically observes the scattering of photons that are emitted at either higher or lower energy corresponding to excitation or relaxation of the vibrational modes of a molecule. These photons emitted through inelastic scattering only occur at a rate of 1 in 10^6 - 10^{10} incident photons, yielding a Raman signal up to several orders of magnitude smaller than that of fluorescence. [2,3] Though developments in laser and photodetector technologies have aided in the applicability of Raman scattering in analytical instrumentation, continued advancements in this field are necessary due to the low sensitivity of Raman scattering instruments. [3]

Surface-enhanced Raman spectroscopy was a discovery made by Martin Fleischmann in 1974 and theoretically explained by Jeanmaire and Van Duyne in 1977 that noted the enhancement of Raman signal for adsorbates on rough metal substrates. [4,14] Major features of the SERS enhancement are its dependence on the nanostructure of the particle involved and on the polarizability of the sample material. [5,6] The

surface-enhancement interaction between the adsorbate and the substrate can be broken into two subcategories: the electromagnetic mechanism (EM) of the enhancement, of which many theories and understandings exist, and the chemical mechanism (CM) of the enhancement, which is less understood due to its smaller effect on the enhancement. [13] Comparatively, the enhancement factor, *EF*, of the EM is approximately 10^6, whereas enhancement from the CM is 10^1-10^2. At a metal nanoparticle surface, the EM interaction between the electric field vector of light and the surface plasmon of a metal sphere of material may generate an oscillating electromagnetic field that is amplified as compared to either constituent. [5,6] If the frequency of the incident light is in resonance with the collective oscillation of the valence electrons of the metal material, this is known as localized surface plasmon resonance (LSPR). [5] The effects of this interaction can be seen in Fig. 1.1.

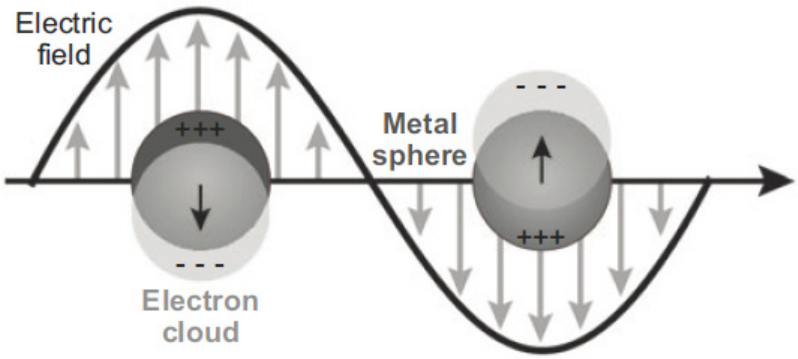

Figure 1.1: The localized surface plasmon resonance between the incident light and collective nanoparticles [5]

The excitation of the LSPR gives rise to the specific absorption and scattering of resonant radiation and the generation of electromagnetic field at areas of roughness. [3]

The electromagnetic enhancement between the incident electromagnetic field and an isolated sphere of material can be understood with the proportionality shown in Eq. 1.1.

$$EF = \frac{|\mathbf{E}_{\text{out}}|^2 |\mathbf{E}'_{\text{out}}|^2}{|\mathbf{E}_0|^4} = 4|g|^2|g'|^2 \qquad \text{(Equation 1.1) [5]}$$

where *EF* is the SERS enhancement factor, E_{out} is the electromagnetic field outside of the particle, E_0 is the incident field intensity, and *g* is defined as $g = \frac{\varepsilon_{in} - \varepsilon_{out}}{(\varepsilon_{in} + 2\varepsilon_{out})}$. Maximum enhancement is observed at the largest value of *g* such that the wavelength-dependent dielectric constant, $\varepsilon_{in} \approx -2\varepsilon_{\text{out}}$. For coinage metals, such as silver and gold, this is achieved in the visible and near-IR. [3] At small Stokes shift, *g* and *g'* are at approximately the same wavelength and *EF* scales with a factor of g^4. Further study of this theoretical model can be found through Kerker *et al*. [7]

In recent years, SERS has found use as an analytical device ranging from detection of anthrax, glucose sensing, prostrate-specific antigen, pesticides and explosive agents. [8,9,10,11,12]

1.2 Thin Films Deposition for the Enhancement of Raman Scattering

Interest in the biological and chemical sensing properties of surface-enhanced Raman spectroscopy revolve around the variety of substrates that yield amplification of Raman signals. Typically, substrates for SERS consist of noble metals, such as gold, silver, or copper. [15] Silver absorbs strongly within the visible region of light and experimentally has been determined to hold an absorption maximum between 465 – 600 nm. [16] The absorption maximum, however, is known to shift with dependence on nanoparticle size. With similarly shaped nanoparticles, silver nanoparticles have been

determined to red-shift with increasing size. [15] Nanoparticle shape and laser wavelength also have a part in determining the absorption maximum for a given material.

Reproducible tuning of metal nanoparticle size plays a large factor in the determination of optimal absorption for surface-enhanced Raman spectroscopy. Novel studies have been explored which investigate the formation of tunable silver nanoparticle spacing with temperature, [17] the fabrication of controllable silver grain sizes through air-dried silver coatings, [18] and the specific synthesis of shaped silver nanoparticles through use of an anodic aluminum oxide substrate. [19] Though prior studies have mainly focused on the noble metals Au, Ag, and Cu, Tian *et al.* have developed SERS on net transition metals, such as Pt, Ru, Rh, Pd, Fe, Co, Ni, and alloys of the like. [20] However, current studies have lacked sufficient observation and experimentation on aluminum thin films for SERS enhancement. Aluminum yields an LSPR within the deep ultraviolet optical range for small particles. [21] The abundance of aluminum as compared with the noble metals increases its appeal as a promising substrate for SERS. Studies have been made on the red shift effects of triangular aluminum nanoparticles [22] and the tailoring of the LSPR shifts with aluminum nanorod antennas and nanodisks. [23,24,25] A major focus of this study is the deposition and LSPR tuning of aluminum nanoparticles sizes into the optically visible region for SERS through variations in deposition thickness and deposition temperature.

CHAPTER TWO

Methods and Materials

2.1 Chamber Setup

Thin films were fabricated in high vacuum with a custom vacuum chamber at Baylor University. The vacuum chamber, shown in Fig. 2.1 and Fig. 2.2, was equipped with two sources for evaporation: a thermal evaporator and an electron beam evaporator. A schematic of the chamber is shown in Fig. 2.3. The chamber was brought to vacuum by a Varian SD-91 rotary pump and a Varian Turbo-V 250 turbopump. Vacuum pressures were measured by a hot-filament ionization gauge and samples were mounted onto a rotatable two-pronged sample stage. All experiments were conducted in high vacuum with pressures ranging from 1×10^{-5} Torr to 1×10^{-7} Torr. The chamber was vented with nitrogen gas when sample transfer was required.

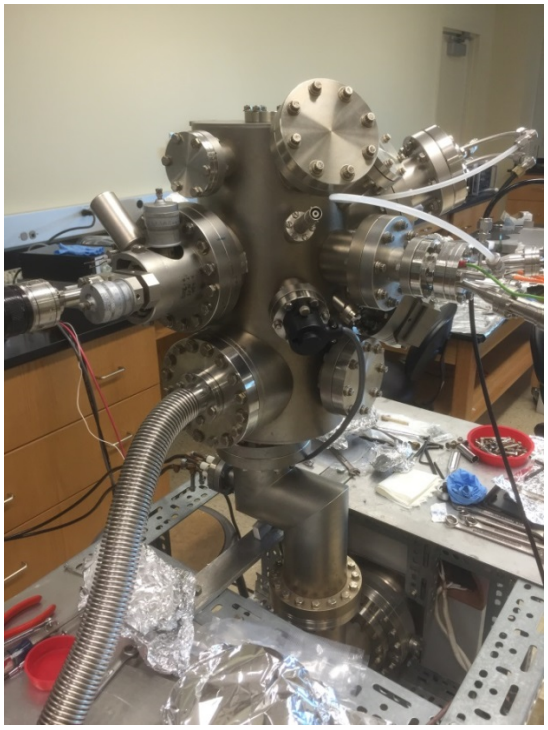

Figure 2.1: The evaporation vacuum chamber with a thermal evaporator and electron beam evaporator

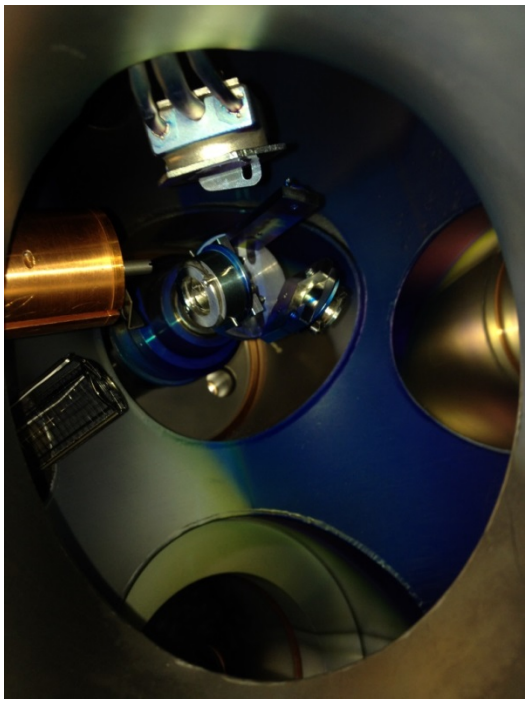

Figure 2.2: View of the inside of the vacuum chamber

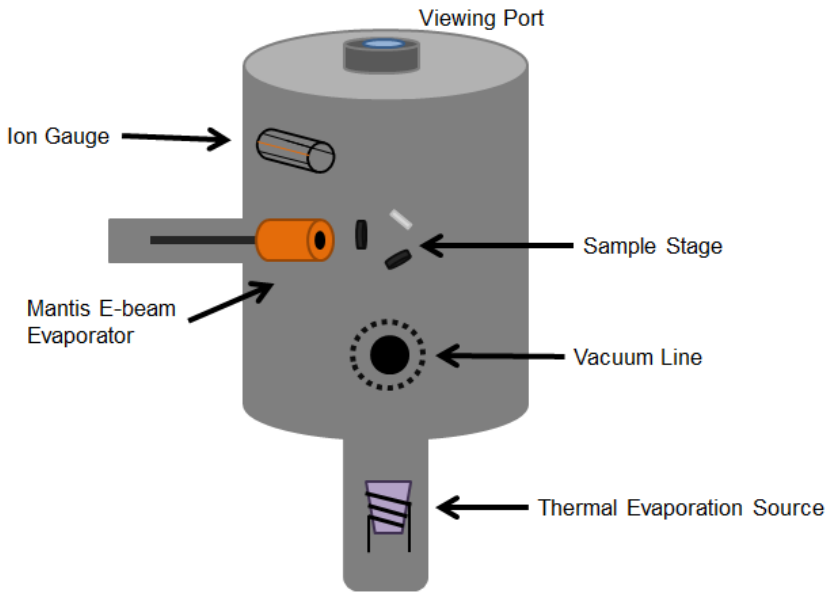

Figure 2.3: Schematic of the vacuum chamber with two evaporation sources

2.2 Sample Preparation

2.2.1 Glass

Precleaned, plain white glass microscope slides (75 x 25 x 1 mm, VWR) were etched with an Agilent diamond tipped pencil and partitioned into twelve equivalent sections. The sections were run through three fifteen minute cycles of cleaning with a VWR ultrasonic cleaner as shown in Appendix Fig. 2.2.1. The partitioned glass samples were submerged into a 400 mL glass beaker filled with 50 mL of acetone and the machine was allowed to run the first cycle. The second and third cycles consisted of 50 mL of ethanol as shown in Appendix Fig. 2.2.2. The glass slides were then dried with nitrogen gas.

2.3 Thermal Evaporation

Thermal evaporation, synonymous with resistance evaporation, is a technique in which chemical material is vaporized through radiative heating from an electric filament

in contact with crucibles of low vapor pressure and high melting temperature. These specific crucibles prevent chemical interactions between the crucible and source material and allow for high purity evaporations. The evaporations are run in high vacuum to prevent chemical reaction with atmospheric substances. As the thermally energetic material vaporizes, contact with the lower temperature substrate causes deposition, the direct transition of the material from the gas phase to the solid phase. This allows for very precise synthesis of thin films on a wide range of substrates.

2.3.1 Preparation of Copper Phthalocyanine Thin Films

Copper phthalocyanine (CuPc) thin films were prepared by physical vapor deposition (PVD) growth. CuPc powder was loaded into a boron nitride crucible as shown in Fig. 2.4 and Fig. 2.5. The crucible was heated by a tungsten wire basket which was connected to a current-controlled power source. The current and voltage from the power source and the pressure within the chamber were monitored throughout the thermal evaporation experiments. The power was slowly ramped up to specified currents to allow for steady outgassing with the sample facing away from the source. The typical evaporation current was around 18.0 A with a 40 minute warm-up period. At evaporation temperatures, sample substrates were turned to face sources. Deposition times ranged between 5 to 20 minutes at pressures $<2.0 \times 10^{-6}$. Calibration of the evaporation rate was performed after addition of new source powder. The calibrations were visually assessed to determine deposition thickness.

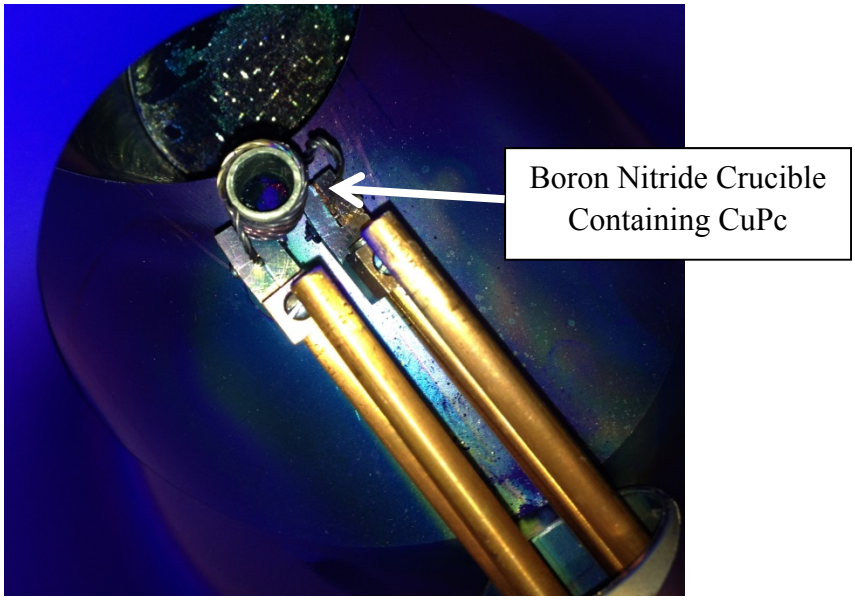

Figure 2.4: Copper phthalocyanine within a boron nitride crucible inside the vacuum chamber

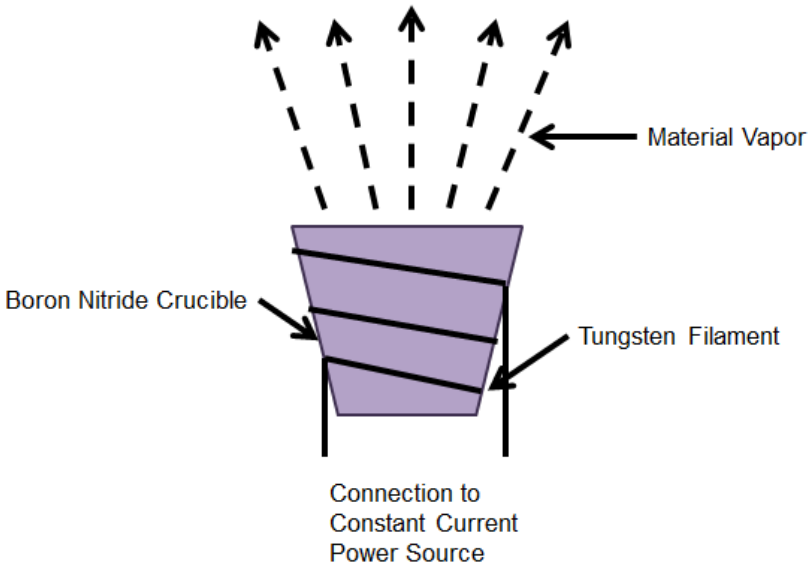

Figure 2.5: Schematic of thermal evaporation source

2.3.2 Fabrication of Thermal Deposition Collimator

Due to the large area of deposition from the CuPc source, a physical collimator was necessary to limit the diameter of deposition. A collimator was fabricated from a used

copper gasket. A section of the gasket was removed and reformed into a 4 cm bar of copper. An 8 mm in diameter hole was drilled into the center of the bar and two more 7 mm holes were drilled on either side of it. The bar was bent 90° in the center of these two holes, which allowed for the collimator to fit two copper feedthroughs which housed the CuPc source and crucible. A thin molybdenum plate was attached to each of the copper collimators, and 4 mm holes were drilled into the center. The first collimator consisted solely of a molybdenum plate covering the opening of the crucible. A second collimator was attached 2 cm above the first and a third collimator was fixed 5 cm above the second, as shown in Fig. 2.6 and Fig. 2.7.

Figure 2.6: Molybdenum collimators attached to a thermal evaporation source

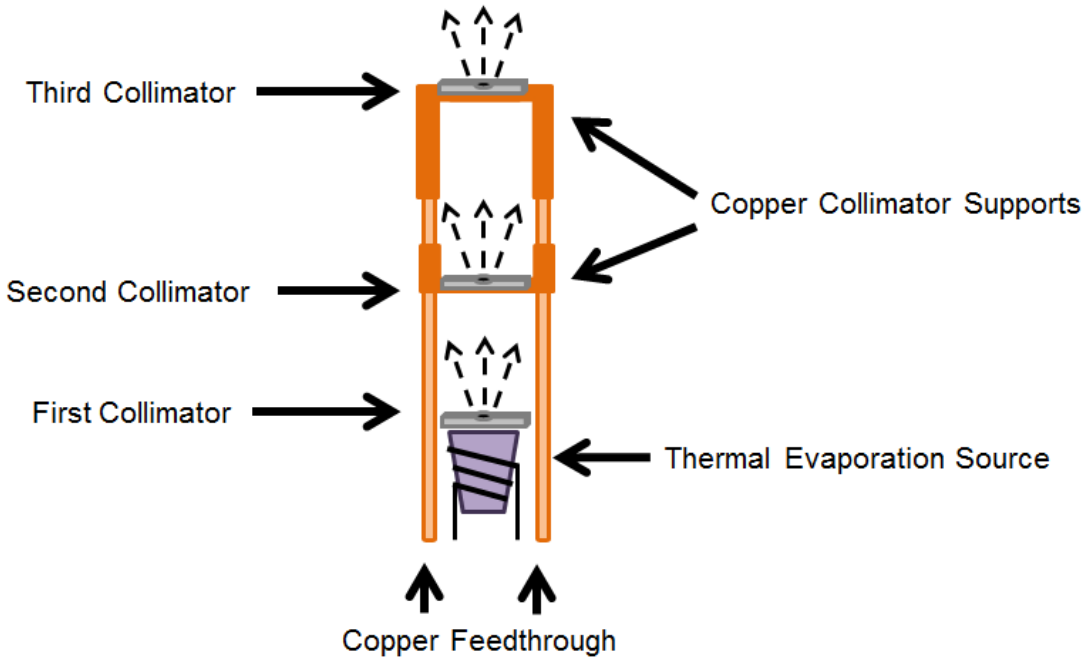

Figure 2.7 Schematic of the collimator setup

2.4 Electron Beam Evaporation

Similar to resistance evaporation, electron beam evaporation relies on heating of chemical material with precision and gradualness. E-beam evaporation differs from resistance evaporation, however, in that the source of heating comes from a stream of electrons emitted by a filament. These electrons bombard source material with the application of a voltage bias that curves the beam of electrons. Heating source material at a specific point with electrons allows for melting and evaporation of a large number of chemical materials. Substrates, at a lower temperature as compared with the evaporation source, allow for precise deposition of source material. Growth of thin films occurs on the nanometer scale, typically ranging between 50 to 200 Å.

2.4.1 Preparation of Aluminum Thin Films

Aluminum thin films were synthesized by deposition of aluminum with a Mantis M-EV Electron Beam Evaporator, shown in Fig. 2.8 and Fig. 2.9. The aluminum source was either an aluminum rod or 99.97% aluminum powder within a pyrolytic boron nitride liner. The filament current, high voltage power, and flux from the power source and the pressure of the chamber were monitored and recorded during all evaporations. Temperature within the electron beam gun was kept stable with water cooling at 15°C. The electron gun was allowed to outgas for 10 minutes with current at 2.00 A with source high voltage off. After sufficient outgassing, the filament current was ramped down to zero and high voltage power was turned on. The current was then turned up to around 1.80 A and slowly ramped up in 0.1 A or 0.05 A increments. The pressure was allowed to stabilize between increments. Deposition occurred around 2.60 A with variable time ranging from 10 minutes to 40 minutes. Deposition was visually confirmed when samples were removed from the chamber.

Figure 2.8: M-EV Electron Beam Evaporator

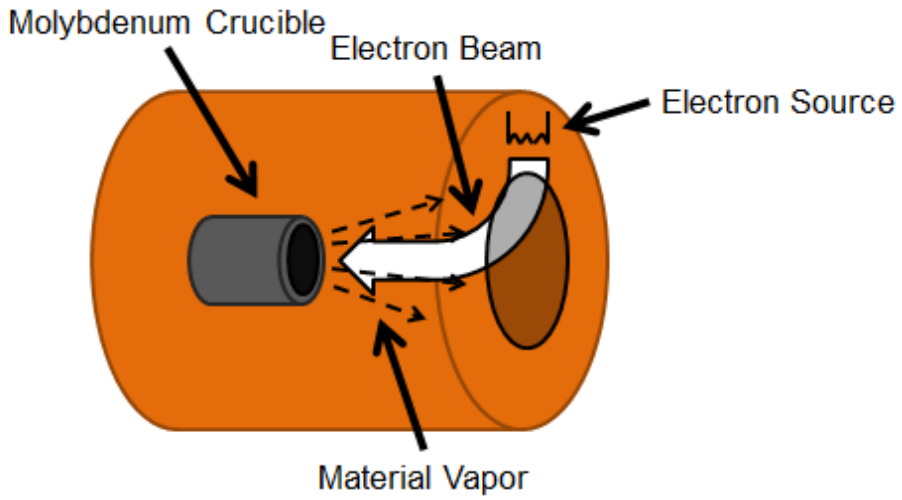

Figure 2.9: Schematic of electron beam evaporator

2.4.1 Preparation of Silver Thin Films

Silver thin films were similarly synthesized by deposition of silver with the Mantis M-EV Electron Beam Evaporator. The silver source was silver pellets (Kurt J. Lesker Company, 99.99%, 1/8'' Diameter x 1/8'' Long) heated within a molybdenum crucible. The filament current, high voltage power, and flux from the power source and the pressure of the chamber were monitored and recorded during all evaporations. Temperature within the electron beam gun was kept stable with water cooling at 15°C. The electron gun was allowed to outgas for 10 minutes with current at 2.00 A with source high voltage off. After sufficient outgassing, the filament current was ramped down to zero and high voltage power was turned on. The current was then turned up to around 1.80 A and slowly ramped up in 0.1 A or 0.05 A increments. The pressure was allowed to stabilize between increments. Deposition occurred around 2.50 A with a deposition time of 10 minutes. Deposition was visually confirmed when samples were removed from the chamber.

2.4.2 Characterization with X-ray Diffraction

X-ray diffraction (XRD) spectra were taken from Siemens D5000 X-Ray Diffractometer, shown in Appendix Fig. 2.4.1. Characterization of homogeneous bulk material with XRD allowed for deposition confirmation when compared with accepted standards. X-rays produced by a cathode ray tube directed towards the sample were diffracted to yield constructive and destructive interference. These diffracted X-rays were then detected and counted and their intensity at different 2θ angles was plotted. Because each crystalline material has a different characteristic X-ray pattern, XRD is utilized in the determination of compound identification.

2.4.3 Characterization with Scanning Electron Microscope

Scanning electron microscopy (SEM) was used to determine the surface topography of a sample. Images were obtained with a FEI Versa 3D DualBeam SEM, as shown in Appendix Fig. 2.4.2. Emission of electrons by a field emission electron source onto a sample provides information of the secondary particles such as secondary electrons and back scattered electrons. By changing characteristics of the electron beam and the detector, variable images of a morphological surface can be obtained. The most relevant variables to this study were the high voltage power (HV), magnification, spot size, and working distance (WD). For comparison, all images were taken at 200,000X magnification.

CHAPTER THREE

Results and Discussion

3.1 Thermal Evaporation

3.1.1 Collimating the deposition width of copper phthalacyanine

To test the effectiveness of the installed collimator in reducing the deposition beam size of evaporated CuPc, experiments with and without the collimator were conducted. The deposition of copper phthalacyanine (CuPc) on a sample-transfer fork is shown in Fig. 3.1. The size of the deposition spot is 50 mm in diameter. A deposition spot size of this magnitude introduces contamination within the evaporation chamber, in which other source material will be evaporated. Therefore, a collimator was designed to reduce the size of deposition to a more reasonable width.

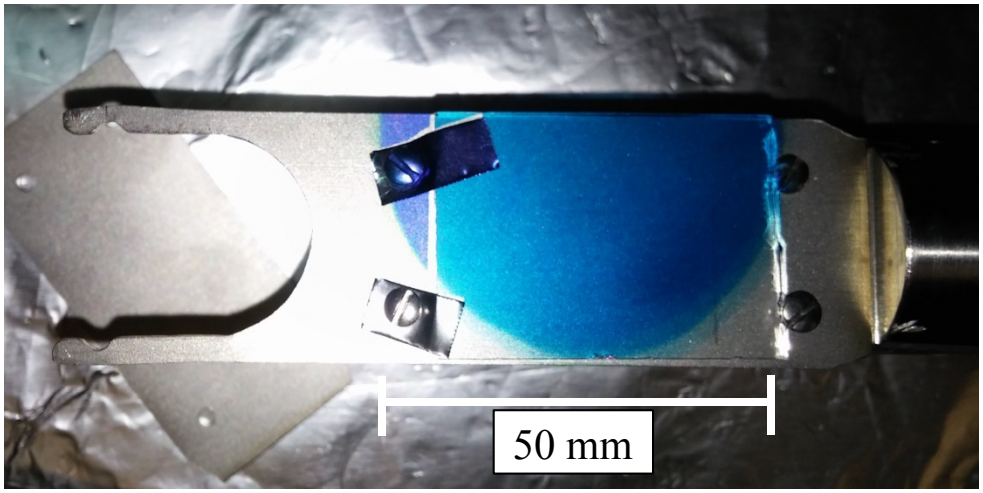

Figure 3.1: Deposition of copper phthalocyanine on a sample transfer fork

A series of collimators were attached above the source crucible, as shown in Fig. 3.2. Use of three collimators allowed for the gradual reduction in size of the evaporant beam. Though initial tests of this collimator yielded promising results, a flaw was observed that hindered evaporation of CuPc onto samples, as shown in Fig. 3.3.

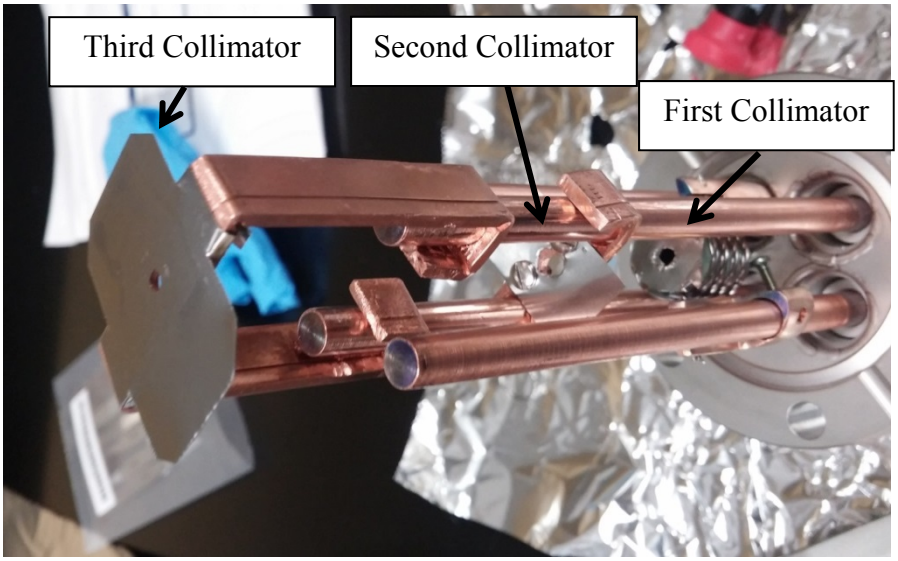

Figure 3.2: The original three collimator setup above the crucible

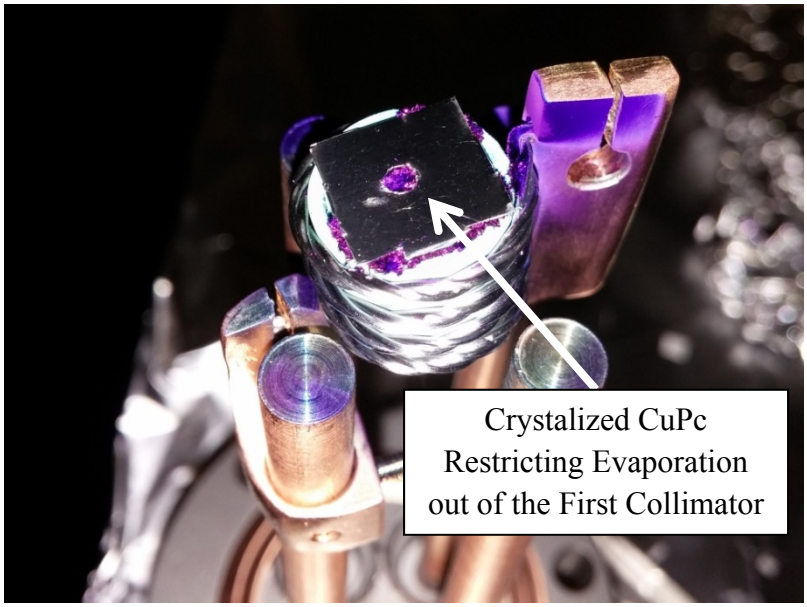

Figure 3.3: The first collimator above the crucible that was clogged by crystalized CuPc

As CuPc was heated and began evaporating, a buildup of CuPc crystals grew on the first collimator. This led to the complete blockage of the first collimator by crystalized CuPc. Crystallization of evaporant CuPc onto the first collimator may have been due to a temperature difference between the heated crucible and source material and the cooler temperature collimator, allowing for deposition of CuPc onto the collimator rather than passing through and depositing onto the substrate. The size of the collimator may have restricted outflow of CuPc gas which accumulated in the complete blockage of the collimator. The removal of this first collimator yielded favorable results, as shown in Fig. 3.4. The final width of this spot was 4 mm in diameter, an acceptable size for future experimentation.

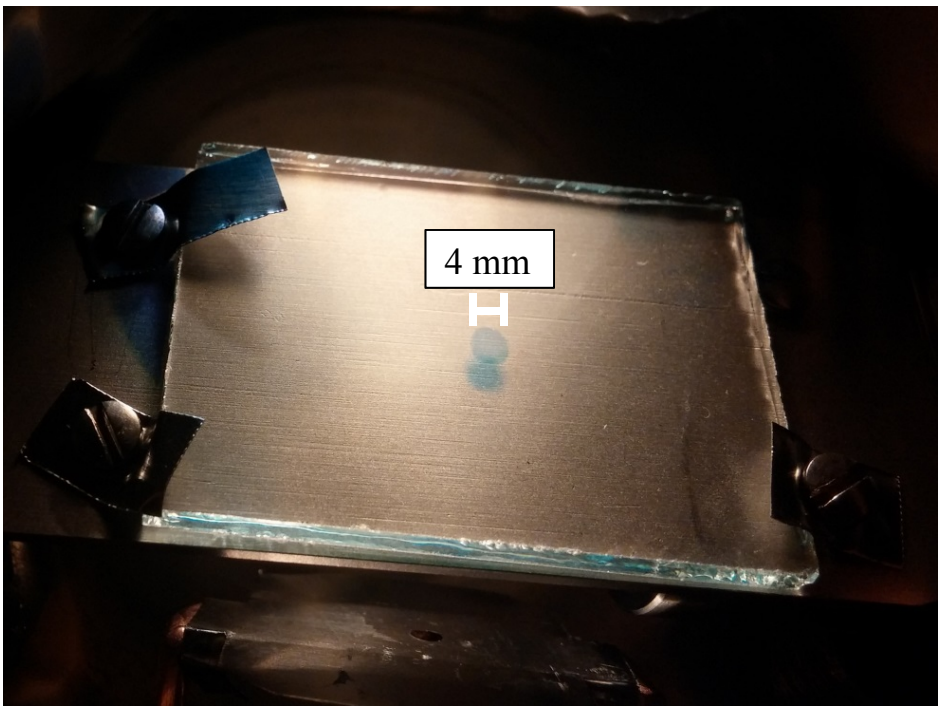

Figure 3.4: Deposition of collimated CuPc on glass

3.2 Electron Beam Evaporation

3.2.1 Deposition of Silver Thin Films

Silver thin films were successfully deposited onto glass substrates. Examples of successful depositions are shown in Fig. 3.5.

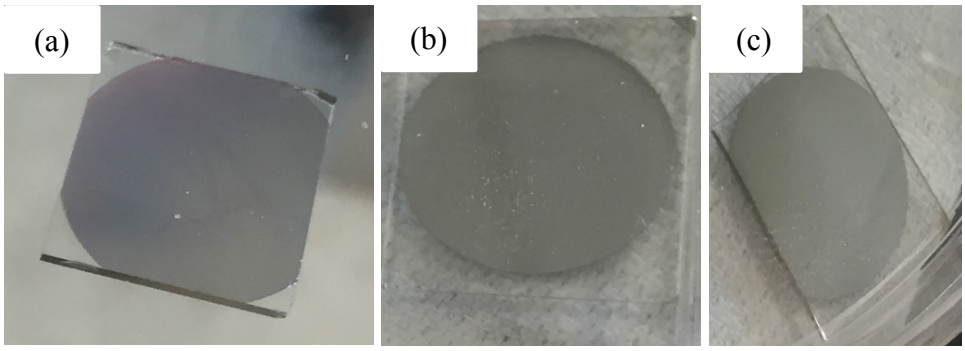

Figure 3.5: Visible deposition of silver thin film: (a) Sample 1 deposited at room temperature for 10 minutes with flux reading on average at 174.1 nÅ , (b) Sample 2 deposited at room temperature for 10 minutes with flux reading on average at 176.1 nÅ, and (c) Sample 3 deposited at 174.4 °C for 10 minutes with flux reading at 194.5 nÅ

Depositions were conducted with comparable variables. Flux, deposition time, and deposition pressure were similar between each deposition. A thickness difference was noted between sample 1 and samples 2 and 3. A possible explanation for this variation may be the angle of the substrate with respect to the metal source. Differences in deposition thickness and deposition temperature led to notable trends in nanoparticle size and morphology.

Graphical representations of two cycles of silver deposition are shown in Fig. 3.6.

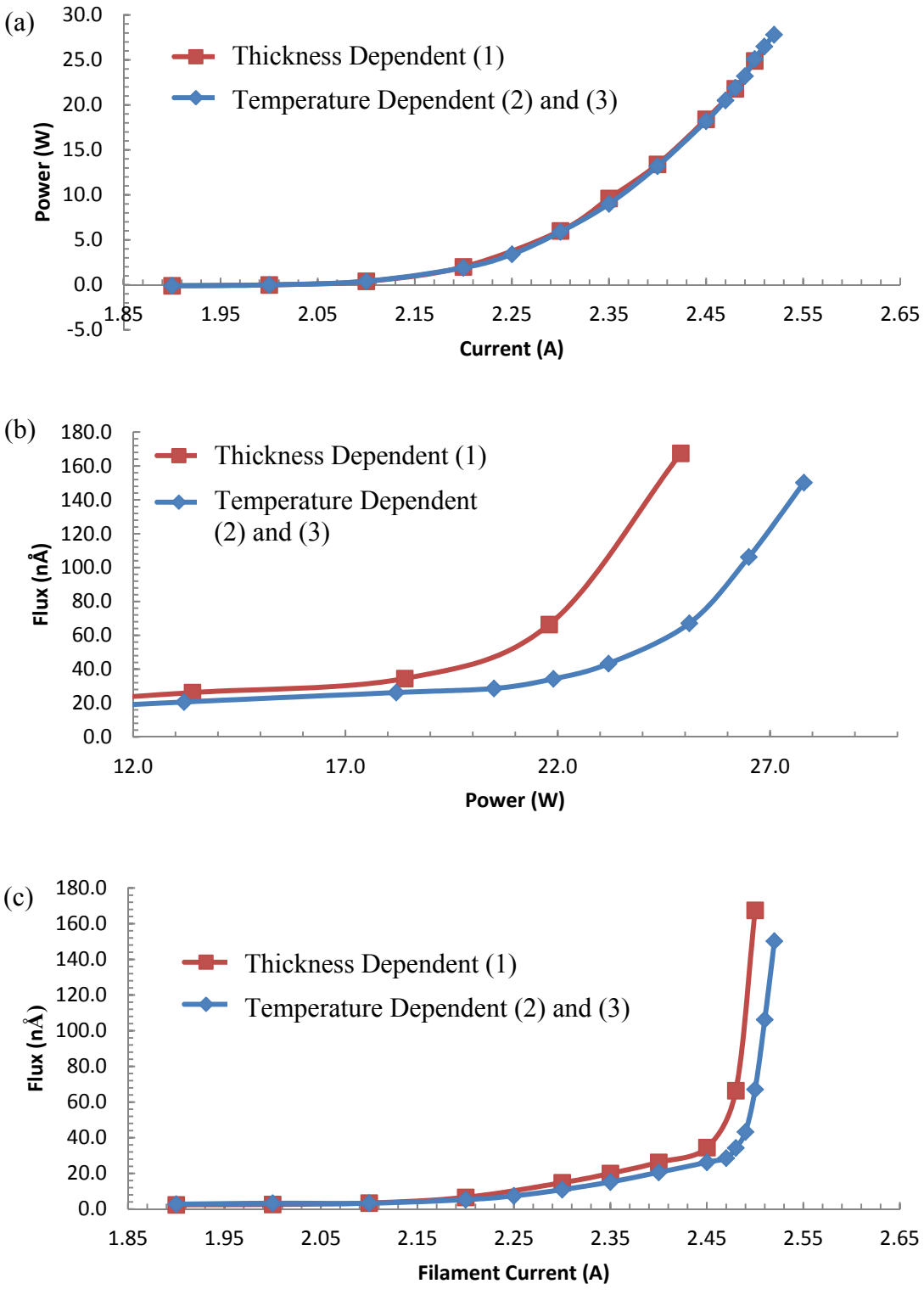

Figure 3.6: (a) Filament current vs. High Voltage (HV) power, (b) HV power vs. ion flux, and (c) filament current vs. ion flux for the three samples shown in Fig. 3.5

Sample 1 was run separately from samples 2 and 3, which were run consecutively within the chamber. The data represents the slow ramping of the power source before evaporation occurs. Items of note are the stability of the filament current vs. power graph in Fig. 3.6 (a) and the rapid increase in the power vs. flux graph as well as the filament current vs. flux graphs of Fig. 3.6 (b) and (c). The rapid increase of these latter two graphs at around Filament Current = 2.45 A and P = 20.0 W indicate the beginning of evaporation. A possible explanation for the differences observed in the latter two graphs may be variation in the interaction between the electrons emitted by the filament and the metal surface. Because samples 2 and 3 were run at a different day and after evaporation of sample (a), less material may have been present within the crucible, therefore requiring higher energy input to reach comparable deposition levels. Variation of the flux between the melting processes of sample 1 and samples 2 and 3 may also account for the differences of the melting curves.

3.2.2 Confirmation of silver with energy-dispersive X-ray spectroscopy

Deposition of silver was confirmed with energy-dispersive X-ray spectroscopy, as shown in Fig. 3.7 and Fig. 3.8.

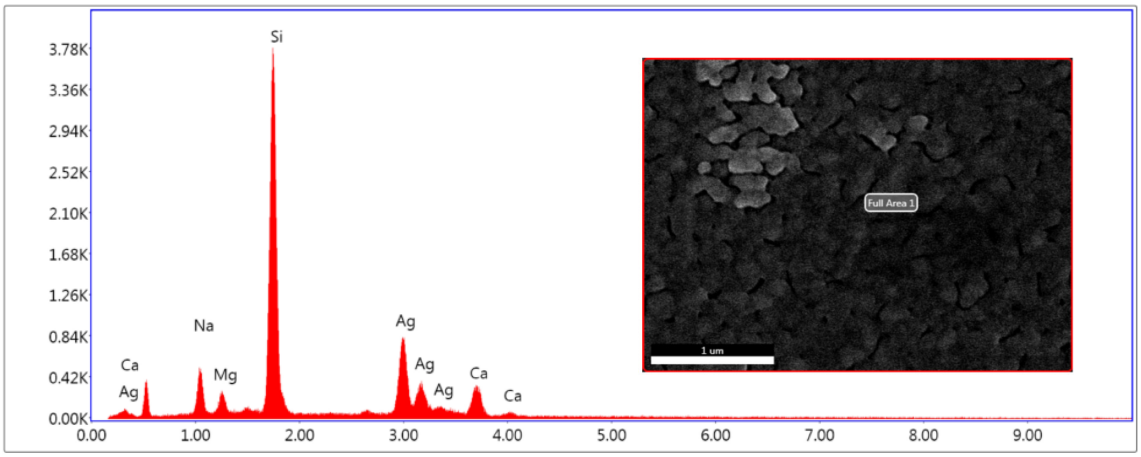

Figure 3.7: EDS spectra of a thick area of Ag-thin film sample #3

Table 3.1: eZAF Smart Quant Result with the relative weight percent of various constituents on thin film sample (c)

Element	Weight %	Atomic %	Net Int.	Error %	Kratio	Z	R	A	F
NaK	10.03	15.97	193.05	9.93	0.04	1.08	0.92	0.38	1.01
MgK	3.33	5.01	98.25	11.40	0.02	1.1	0.93	0.45	1.01
SiK	45.70	59.54	1,948.08	4.75	0.34	1.09	0.95	0.68	1.01
AgL	31.18	10.58	513.61	3.87	0.24	0.82	1.16	0.93	1.02
CaK	9.76	8.91	227.70	6.85	0.08	1.04	0.99	0.76	1.01

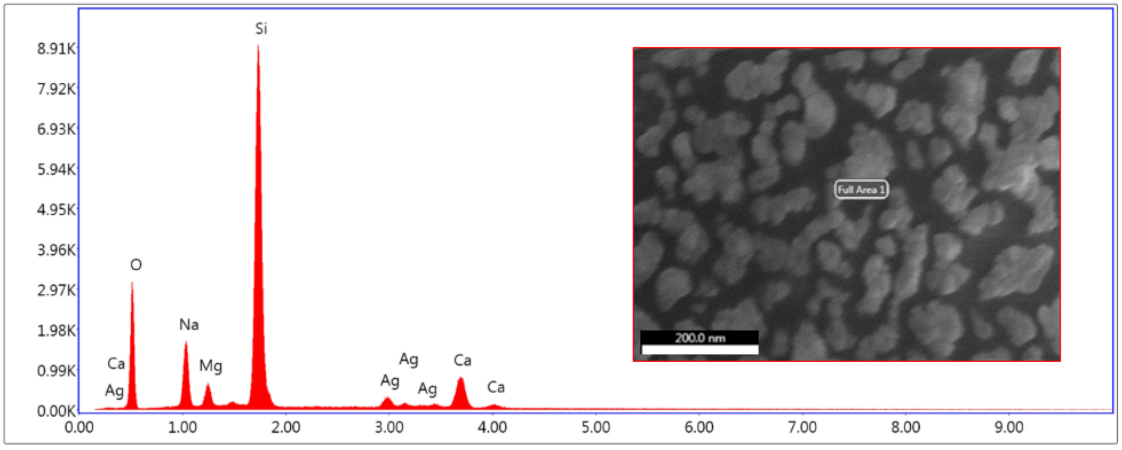

Figure 3.8: EDS spectra of a thin area of Ag-thin film sample #1

Table 3.2: eZAF Smart Quant Result with the relative weight percent of various constituents on thin film sample (a)

Element	Weight %	Atomic %	Net Int.	Error %	Kratio	Z	R	A	F
O K	37.45	51.90	614.76	9.14	0.10	1.07	0.96	0.25	1
NaK	11.77	11.35	421.05	7.83	0.05	0.97	0.99	0.42	1.01
MgK	3.09	2.82	163.83	8.28	0.01	0.99	1	0.48	1.01
SiK	36.90	29.13	2,829.87	4.06	0.26	0.97	1.01	0.72	1
AgL	3.37	0.69	101.03	6.48	0.03	0.73	1.23	1	1.03
CaK	7.43	4.11	349.29	3.79	0.06	0.92	1.05	0.91	1.02

Deposition of silver is confirmed with the presence of the four silver peaks for both spectra. The penetration depth of the EDS probe ranged within the lower micrometer regime, typically under 10 μm. The large peak of silicon on both samples can be attributed to the glass substrate on which the silver was deposited. The extraneous metals present in the spectra can also be attributed to the impurities within the glass. A note of interest is the disappearance of the oxygen peak from the thin sample of samples 1 as compared to the thick sample of sample 3. This may be due in part to the thickness of the silver layer of sample 3 which masked the oxygen present in glass, or SiO_2. Additionally, due to the overlap between the calcium and oxygen peaks, the calcium peak may have masked the reduced oxygen peak. A qualitative comparison of the relative percentages of silver on each sample can be seen in Table 3.1 and Table 3.2. Because the eZAF Smart Quant Result of the EDS had not yet been calibrated when sample spectra were obtained, the shown weight percent and atomic percent are not quantitatively accurate. However, a comparison of the two with each other demonstrates the magnitude of the thickness difference between the two samples, such that the thickness of the sample area of sample (c) yields 31.18 wt% of Ag while the thickness of the sample area of sample (a) yields 3.37 wt% of Ag.

3.2.3 Microstructure of silver thin films with dependence on thickness

A study of nanoparticle size and morphology was undertaken with Ag sample (a). A gradient was noted and thickness-dependent Ag-nanoparticle characterization was explored, as shown in Fig. 3.9.

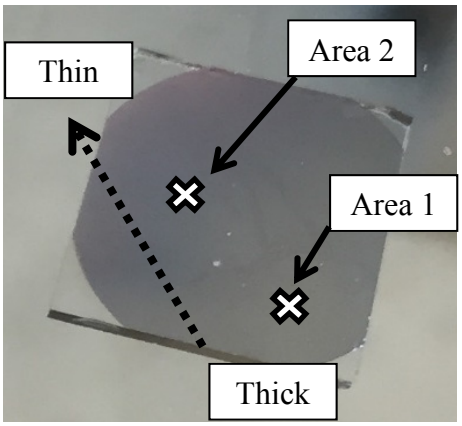

Figure 3.9: Gradient from thick to thin of Ag-thin film sample 1

The SEM morphologies for the two areas shown in Fig. 3.9 are shown in Fig. 3.10.

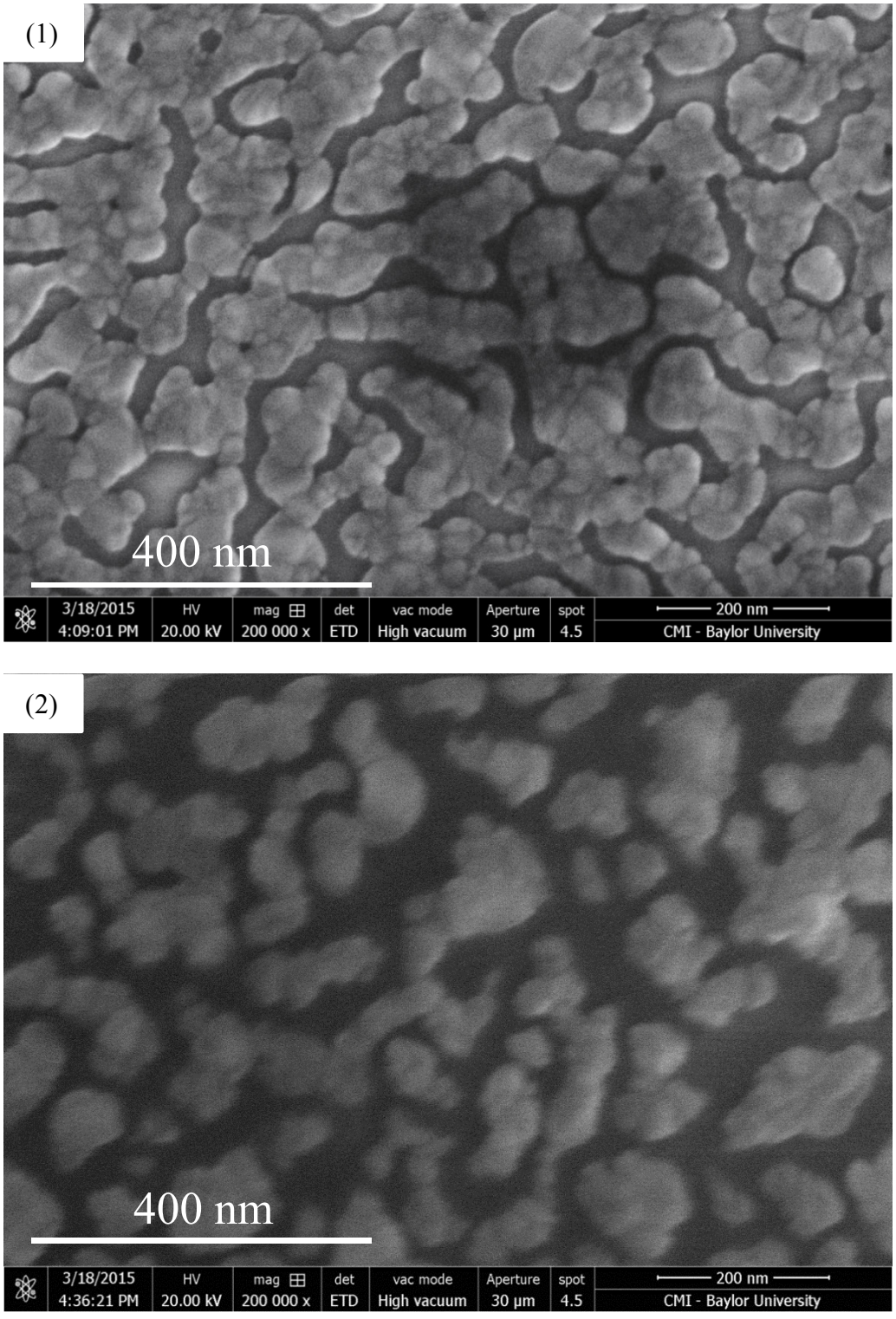

Figure 3.10: SEM images of silver nanoparticle dependence on deposition thickness: (1) thicker area of deposition, (2) thinner area of deposition

Set at the same magnification, the microstructures of the images are different for either thickness. While the island widths range between 30 – 100 nm for both thickness, the densities of islands as well as the interconnection between the islands is dissimilar. Spaces between the islands for the thicker area of deposition are no more than 50 nm wide, whereas the spaces between the islands for the thinner area of deposition are range between 20 – 100 nm. Each observed area was relatively uniform with respect to island shape and size. For both deposition areas, silver seems to follow a Volmer-Weber growth mode, depositing as individually isolated islands rather than fully wetting the surface of the glass substrate. Due to the individual nucleation islands that are seen to form, growth of silver seems to suggest that the interactions between the adatoms of silver are stronger than those between the adatom and the glass substrate. This follows the Volmer-Weber growth mode in that three-dimensional clusters are seen to form, rather than complete wetting or smooth layers of silver on the substrate.

3.2.4 Confirmation of Absorbance Shift of Silver UV-Vis Spectrophotometer

A UV-Vis spectrum of Ag sample 1 was obtained at various thicknesses with a spectrophotometer. The spectrum is shown in Fig. 3.11.

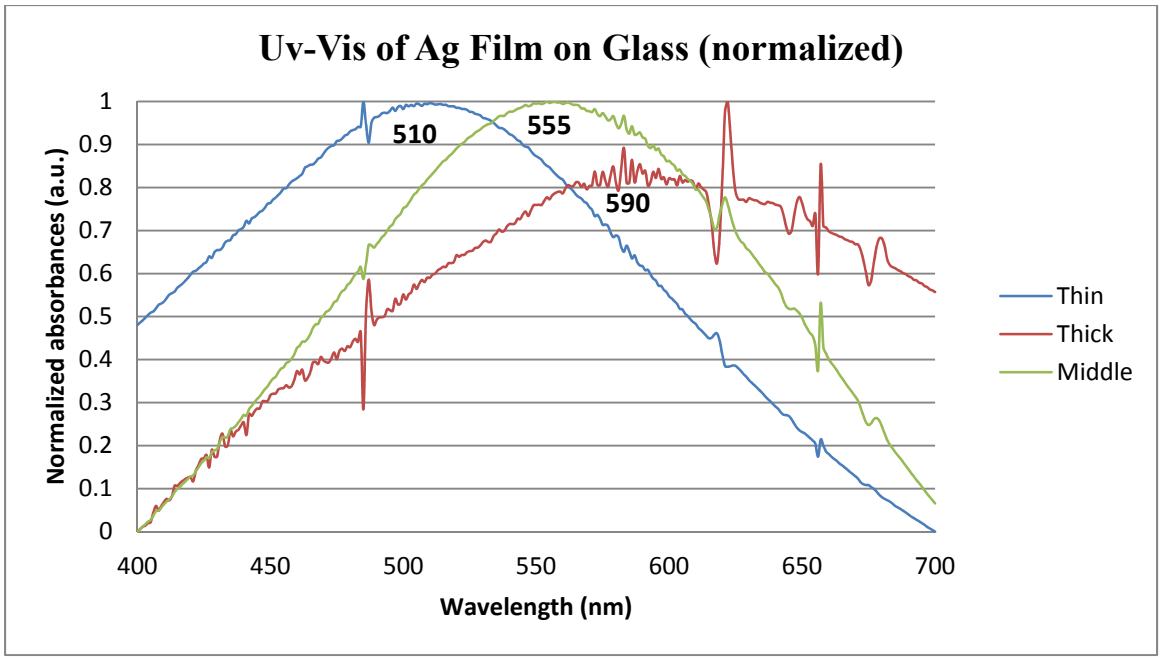

Figure 3.11: UV-Vis spectrum of Ag thin film at different thicknesses

Though the spectrum can only be read quantitatively, it depicts a clear red-shift of the absorption peaks for silver as dependent on silver thickness. For the thickest sample area of silver deposition, an absorption peak at around 590 nm was observed. The thinnest area of deposition yielded an absorption peak at around 510 nm and the intermediate area of deposition yielded a peak at around 555 nm. The successful tuning of silver absorption peak for various deposition thicknesses and nanoparticle densities was therefore confirmed.

3.2.5 Microstructure of silver thin films with dependence on temperature

To determine the effect of the substrate temperature on silver nanoparticle sizes, Ag samples 2 and 3 from Fig. 3.5 were examined. Sample 2 was deposited at room temperature for 10 minutes and sample 3 was deposited at 174.4 °C for 10 minutes.

These two evaporations were consecutively deposited with comparable flux, time, and chamber pressure. Imaged sampled areas are shown in Fig. 3.13.

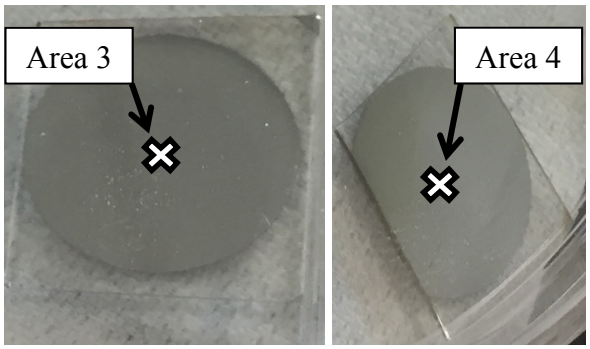

Figure 3.12: Ag thin films deposited on glass at varying temperature: (3) room temperature deposition, (4) elevated temperature deposition at 174.4 °C

SEM images of these two sample areas were explored, as shown in Fig. 3.12.

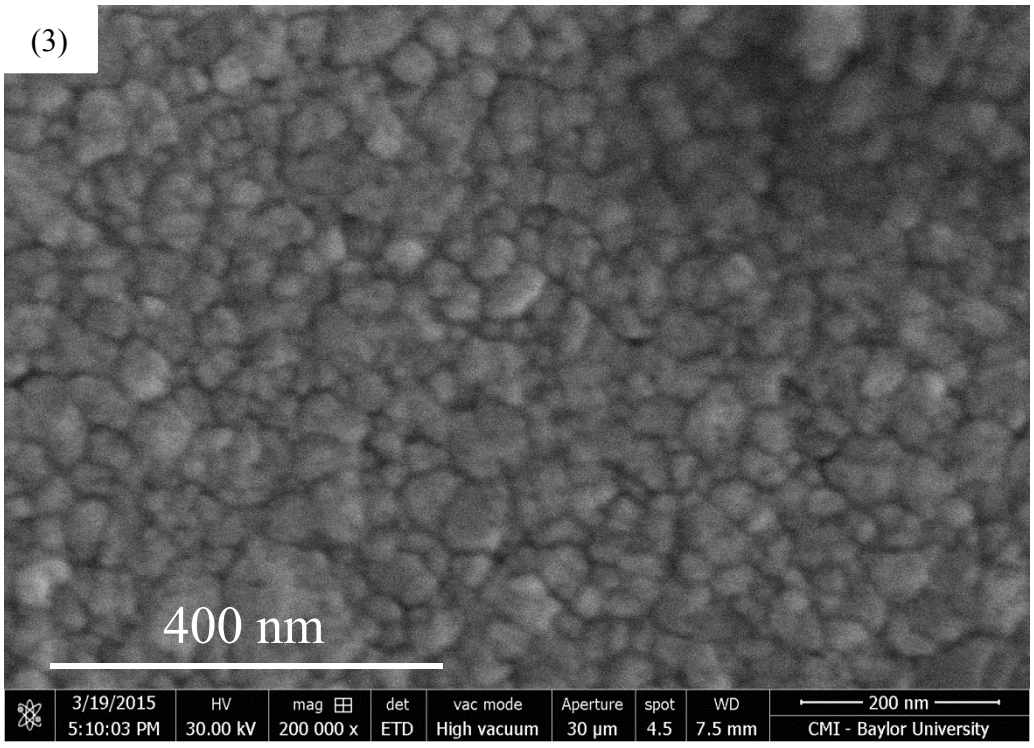

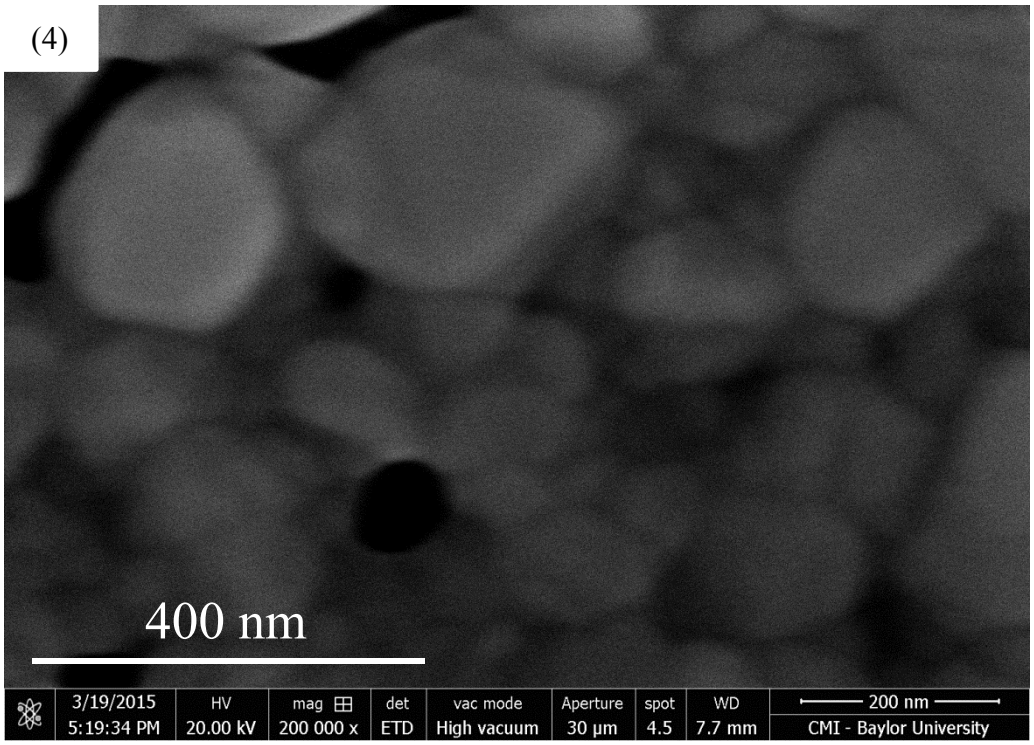

Figure 3.13: SEM images of Ag thin films deposited on glass at varying temperature: (3) room temperature deposition, (4) elevated temperature deposition at 174.4 °C

Deposition of silver with variable temperature yielded very different surface structures for room temperature deposition and elevated temperature deposition. The two depositions were conducted with similar parameters such that temperature difference was the only measured variable between the two samples. The largest difference observed was the size of the nanoparticles. For the room temperature deposition the nanoparticle sizes ranged between 20 – 100 nm. As compared to the elevated temperature deposition, where the nanoparticle sizes ranged between 175 – 200 nm, the room temperature deposition shows a much higher density of more uniform particles. Deposition at 174.4 °C seems to show large aggregates of silver as compared to the individual grains seen in the room temperature deposition. Both the growth modes of the room temperature sample and the elevated temperature sample were observed to follow a Volmer-Weber

growth mode. Similarly to the thickness-dependent silver deposition, the growth of additional silver occurs in the three-dimensional direction rather than forming individual true layers. The growth of both samples seems dependent on the nucleation of nanostructures. A difference, however, is found in the size of the three dimensional structure between the two deposition parameters with the elevated temperature deposition yielding far larger structures as compared to the room temperature deposition. An additional note of interest is the formation of pinholes or pores within the elevated temperature deposition. This however, is not further pursued in this study.

3.2.6 Deposition from Aluminum Rods

Synthesis of aluminum thin films was attempted using an aluminum rod as the evaporation source. Even with slow ramping of the electron beam, no notable flux was observed. At a filament current of I = 3.68 A, far exceeding the point of evaporation, no visible deposition was observed. Rather, along with the unsuccessful evaporation of the aluminum rod source, the rod was catastrophically melted. The melted aluminum rod is shown in Fig. 3.14.

Figure 3.14: Electron beam melted aluminum rod. Note the blackened tip of the rod and the large droplet formed

3.2.7 Deposition from Aluminum Powder

Visible thin films were obtained through use of aluminum powder within a molybdenum crucible and a boron nitride liner. Freshly added aluminum powder within the e-beam evaporator can be seen in Fig. 3.15. Note the ball formation of the melted aluminum beside the freshly added aluminum powder.

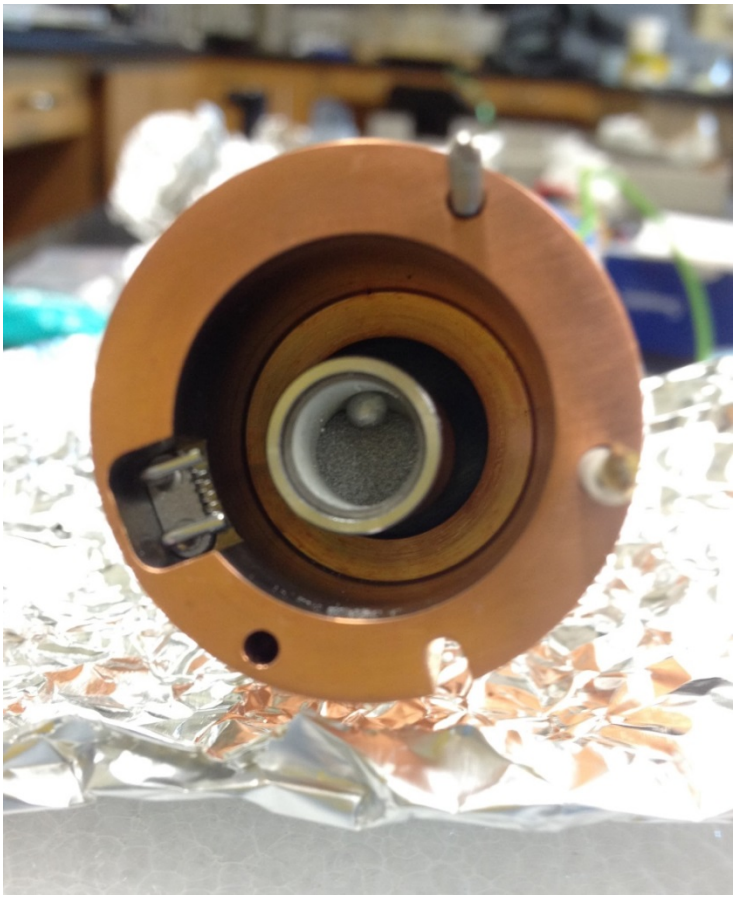

Figure 3.15: Aluminum powder within a boron nitride crucible seated inside the Mantis M-EV Electron Beam evaporator.

Examples of successfully deposited aluminum on glass substrates are shown in Fig. 3.16.

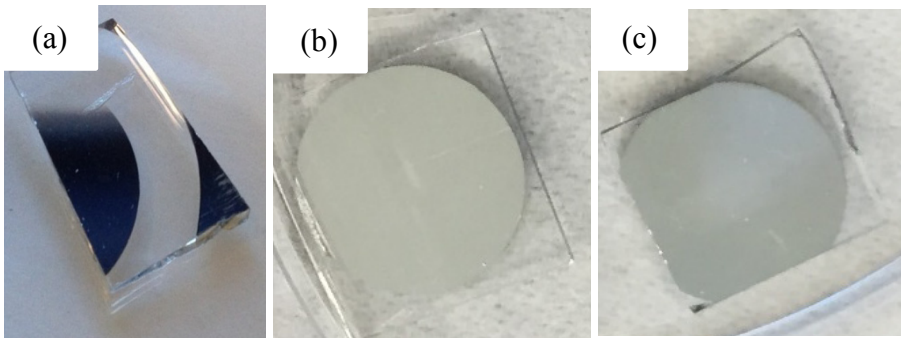

Figure 3.16: Visible deposition of aluminum thin film: (a) Sample #4 deposited at room temperature for 40 minutes with flux reading on average at 138.5 nÅ, (b) Sample #5 deposited at room temperature for 10 minutes with flux reading on average at 143.1 nÅ, and (c) Sample #6 deposited at 174.4 °C for 10 minutes with flux reading at 96.5 nÅ

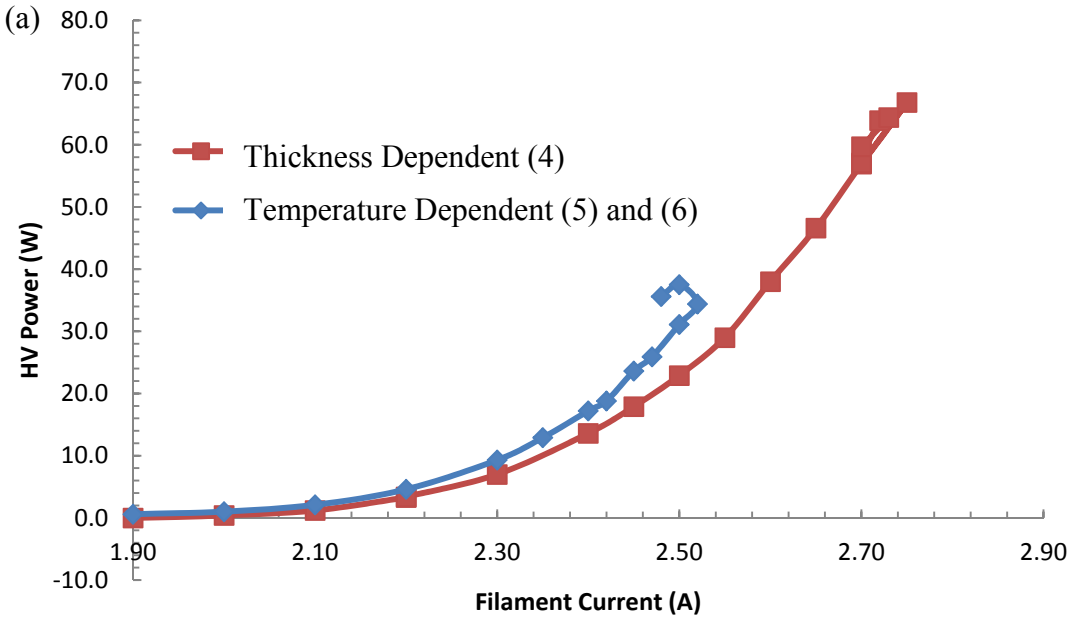

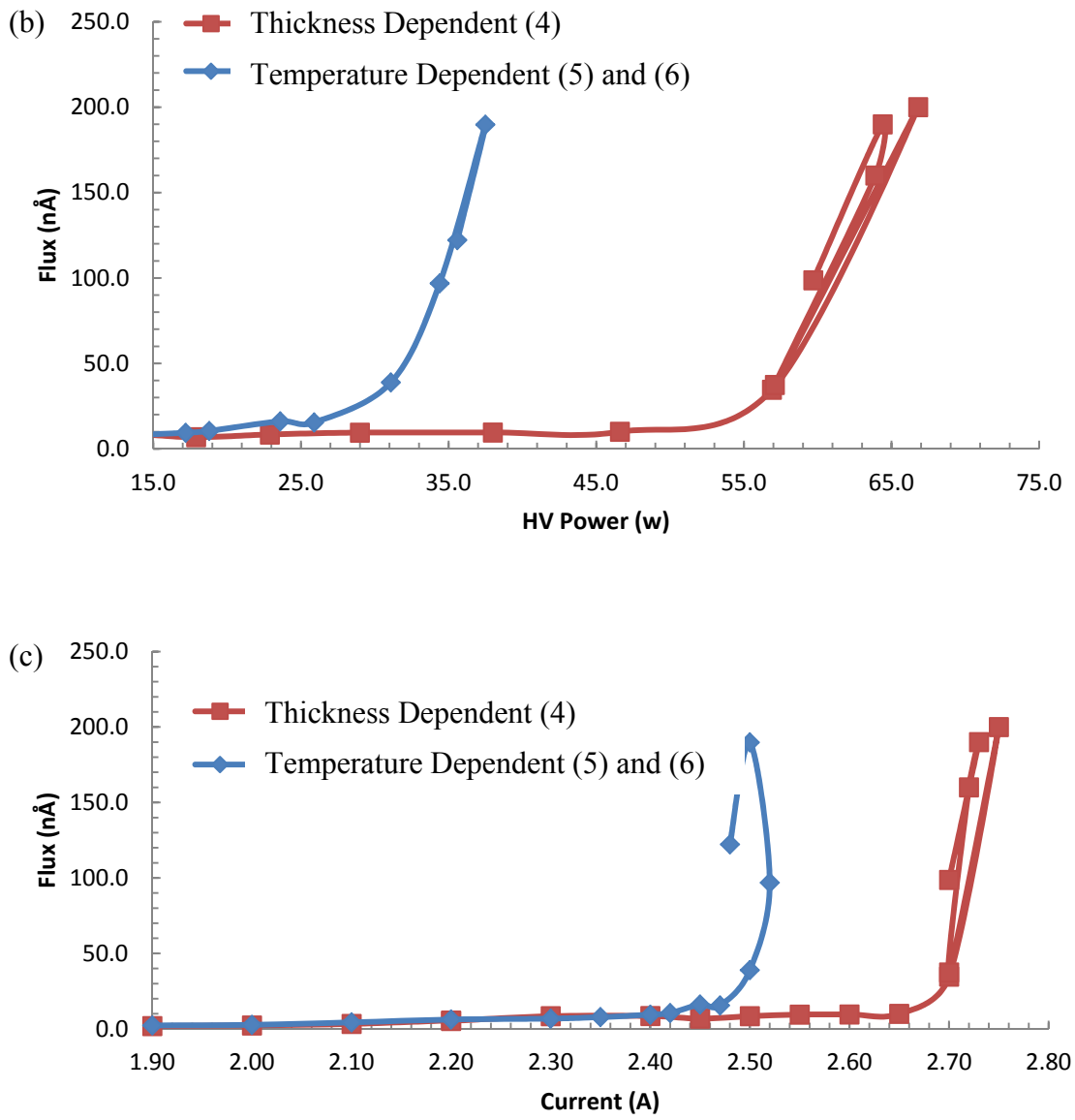

Figure 3.17: Filament current vs. High Voltage (HV) power, HV power vs. ion flux, and filament current vs. ion flux for the three samples shown in Fig. 3.15

Graphical representations of the aluminum depositions shown in Fig. 3.16 are shown in Fig. 3.17. Aluminum sample 4 was run separately from aluminum samples 5 and 6, which were run consecutively within the vacuum chamber. The data represents the ramping from the power source prior to evaporation. The sharp rises in Fig. 3.17 samples 5 and 6 at I = 2.45 A or I = 2.65 A can be attributed to the beginning of evaporation. As

compared to the graphical representations of the silver samples, the aluminum samples are much less stable and require much more careful observation during melting and evaporation. The hook of graphs 3.17 (a) and (c) are due to the lowering of filament current after maximum measurable flux (200.0 nÅ) was reached. Interestingly, for aluminum, the instability of the source led to irreproducible flux at identical filament current. Rather than flux remaining relatively constant at similar filament current, a difference was noted for each cycle of heating. The disparity between the graphs of Al sample 4 and Al samples 5 and 6 is because fresh aluminum powder was added between the two cycles.

3.2.8 Confirmation of Aluminum with energy-dispersive X-ray spectroscopy

Aluminum samples were characterized with EDS, as shown in Fig. 3.18. Corresponding eZAF Smart Quant Results can be seen in Table 3.3.

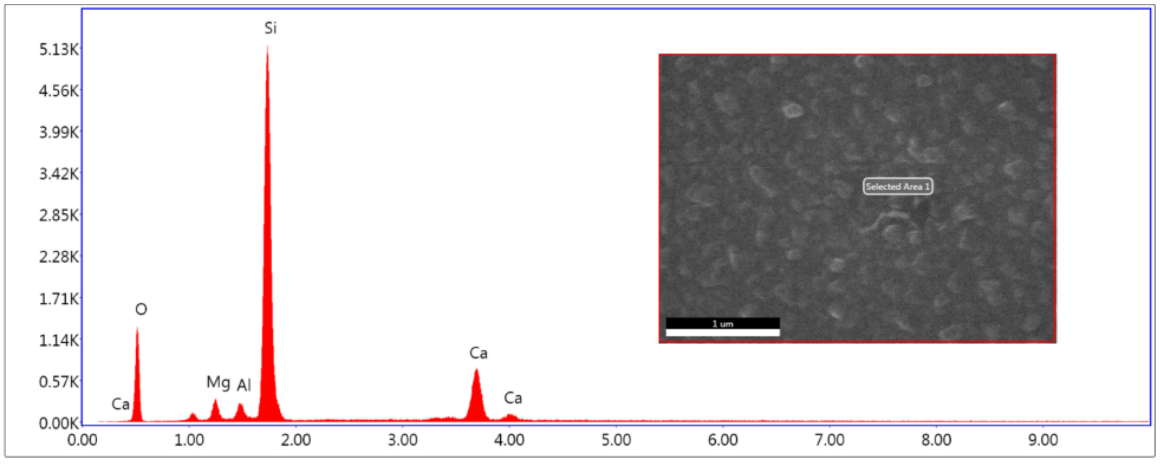

Figure 3.18: Energy-dispersive X-ray spectrum of aluminum sample (c)

Table 3.3: eZAF Smart Quant Result with the relative weight percent of various constituents on thin film sample (c)

Element	Weight %	Atomic %	Net Int.	Error %	Kratio	Z	R	A	F
O K	48.58	63.36	425.67	9.72	0.10	1.04	0.97	0.2	1
MgK	2.69	2.31	107.63	11.18	0.01	0.97	1	0.38	1.01
AlK	1.77	1.37	97.61	10.37	0.01	0.94	1.01	0.5	1.02
SiK	38.27	28.43	2,722.57	4.81	0.23	0.96	1.02	0.63	1
CaK	8.68	4.52	529.40	3.77	0.07	0.92	1.06	0.86	1.02

Elemental evaluation determined the presence of an aluminum peak on visibly deposited areas of the sample. Large peaks of silicon and oxygen can be attributed to the glass sample on which the aluminum was deposited. The existence of sodium and magnesium can be attributed to impurities within the glass samples. The eZAF Smart Quant Results were not yet calibrated with EDAX standards, and therefore may not be representative of actual weight percentages of sampled area.

3.2.9 Confirmation of Aluminum with X-ray diffraction

An XRD spectrum of aluminum deposited on highly ordered pyrolytic graphite (HOPG) and glass is presented in Fig. 3.19. The peaks observed in the XRD spectrum match reference spectrum as shown in Appendix Fig. 3.2.1. The results show that the deposited aluminum is in the polycrystal form and not in the amorphous form. The large peak seen at 55° can be attributed to HOPG. Deposition of aluminum can be confirmed on both aluminum and HOPG.

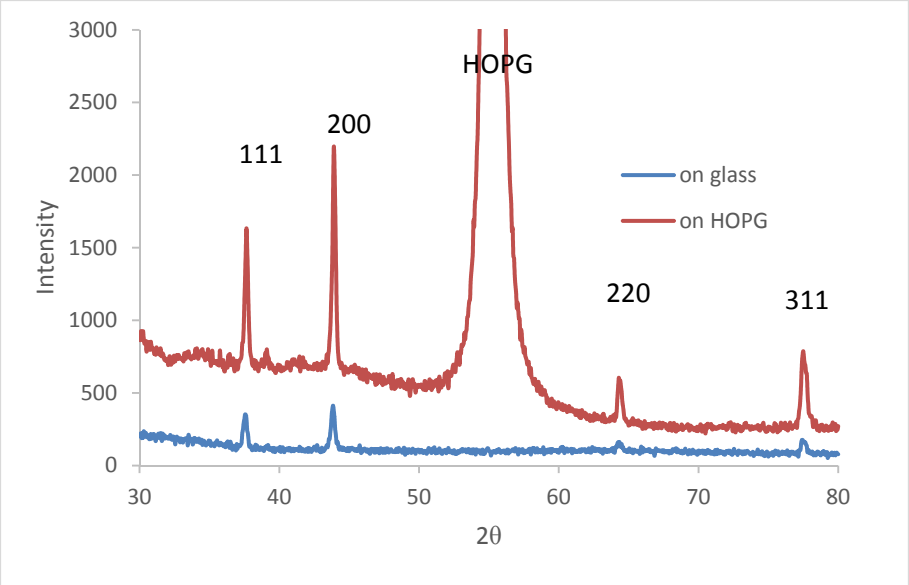

Figure 3.19: X-ray diffraction spectrum for aluminum on HOPG and glass

3.2.10 Microstructure of aluminum thin films with dependence on deposition thickness

A thickness gradient of aluminum was observed with deposition, as shown in Fig. 3.20. The varying thickness was used to determine the dependence of nanoparticle sizes with respect to the thickness of the deposition.

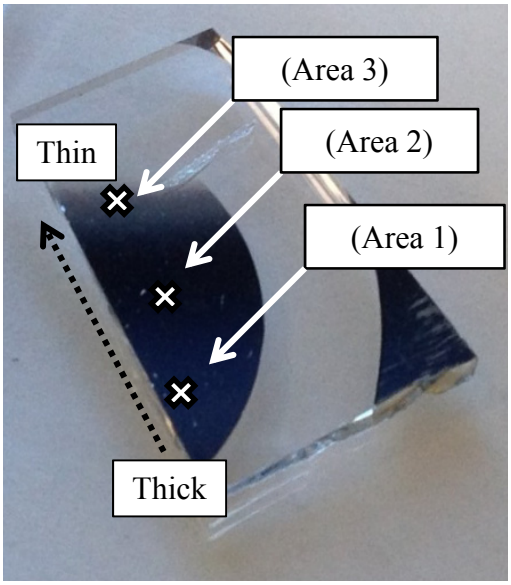

Figure 3.20: Thickness gradient of aluminum on glass, sample 4

The SEM morphologies for three deposition thicknesses on the same sample are shown in Fig. 3.21. Set at the same magnification, the microstructures of the images are greatly different for each thickness. For Fig. 3.21(1), the thickest sample, the nanoparticle sizes ranged between 75 – 200 nm. For Fig. 3.21(2), the intermediate sample, the nanoparticle sizes ranged between 40 – 125 nm. For Fig. 3.21(3), the thinnest sample, the nanoparticle sizes ranged between 10 – 75 nm. The grain sizes for each sample are relatively uniform and a clear trend is observed between the various deposition thicknesses. Therefore, nanoparticle size is dependent on thickness of deposition.

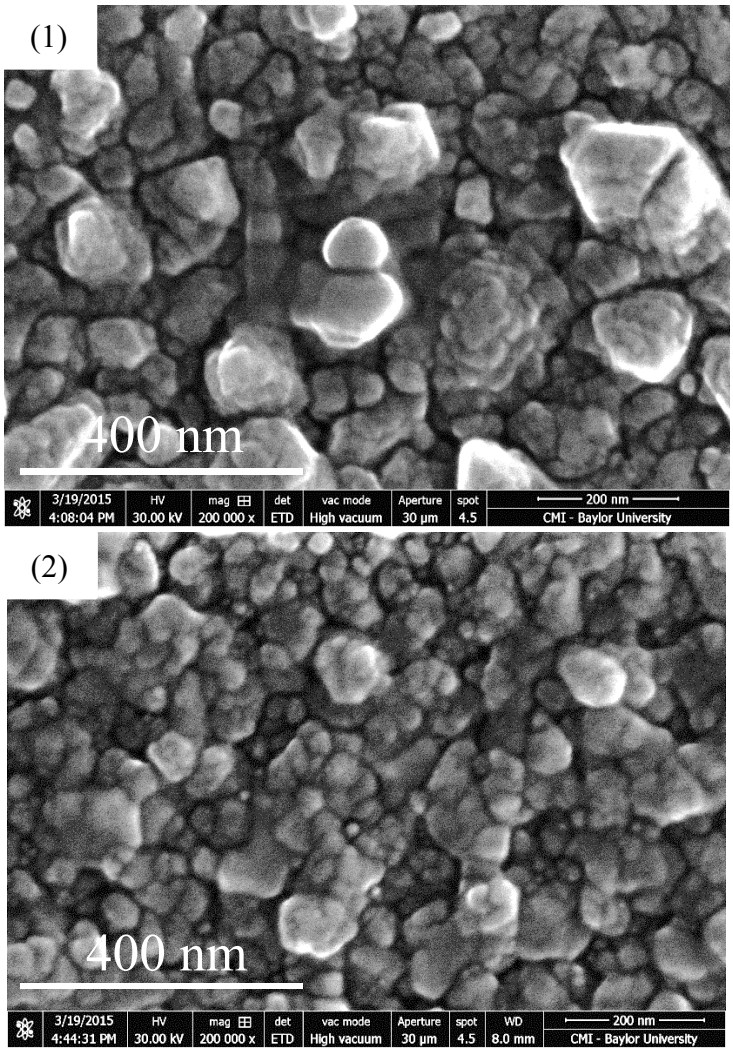

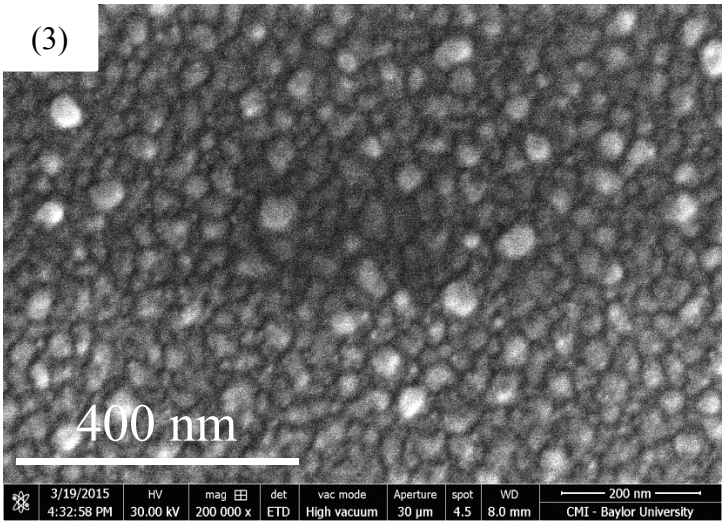

Figure 3.21: SEM images of the surface morphology of three deposition thicknesses of aluminum: (1) thickest sample, (2) intermediate sample, and (3) thinnest sample

3.2.11 Comparison of Aluminum morphology with respect to deposition temperature

Samples (b) and (c) from Fig. 3.15 were studied to determine the nanoparticle size dependence on deposition temperature, as shown in Fig. 22.

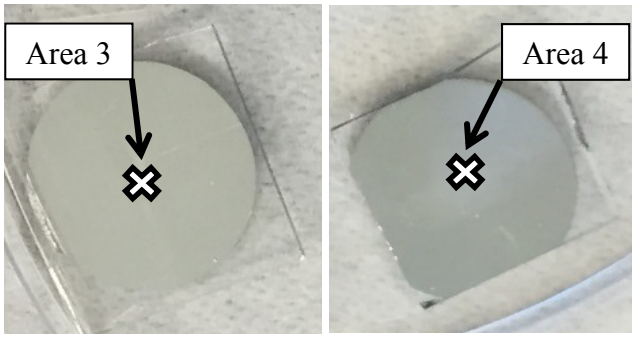

Figure 3.22: Al thin films deposited on glass at various temperature: (3) room temperature deposition, (4) elevated temperature deposition at 174.8 °C

The two aluminum samples were run consecutively within the vacuum chamber to ensure similar environments while depositing. Chamber pressure and deposition time were comparable, but flux for the elevated temperature decreased as deposition occurred.

SEM images of these two sample areas were explored, as shown in Fig. 3.23.

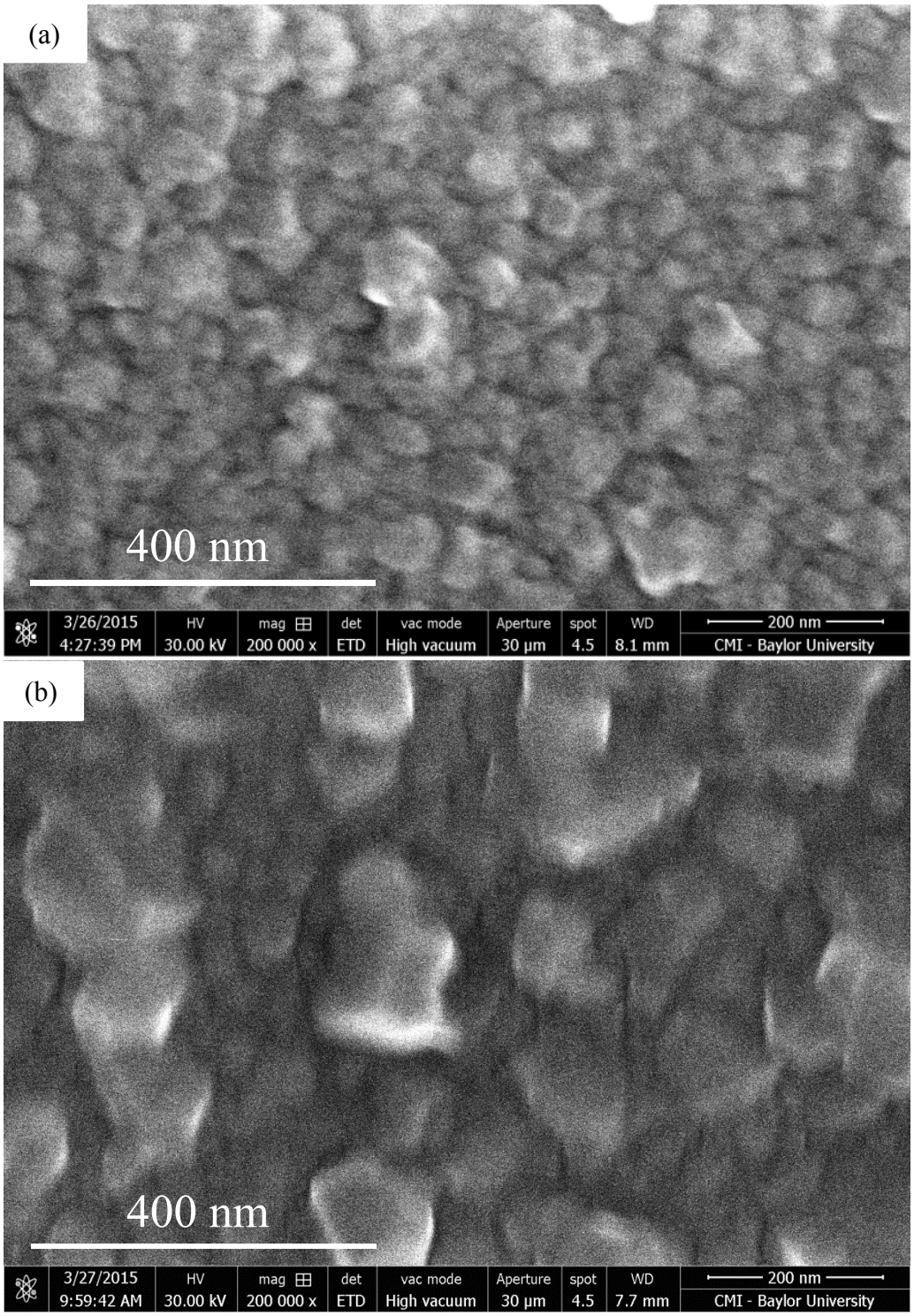

Figure 3.23: (a) room temperature deposition of aluminum, (b) 174.8 °C deposition of aluminum

Differences are observed between samples deposited at room temperature (RT), Fig. 3.23a, and at 174.8 °C, Fig. 3.22b. The grain size of the RT-deposited aluminum particles ranges between 40 – 100 nm and the grain size of the elevated temperature-deposited aluminum particles ranges between 100 – 225 nm. While nanoparticles deposited at RT seem isolated from each other, deposition of aluminum at elevated temperature seems to yield larger particles that aggregate to form larger microstructures. This data is consistent with similar studies of aluminum nanoparticles deposited at different temperatures, as shown in Appendix Figure 3.2.2. [27]

CHAPTER FOUR

Conclusion

4.1 Conclusion

Thin films of CuPc, Ag, and Al were successfully synthesized onto glass microscope slides through thermal and electron beam evaporation. A system of collimators was designed and implemented such that deposition size was reduced for thermal evaporations. Silver depositions yielded thin films that were confirmed visually and analyzed with energy-dispersive X-ray spectroscopy. Silver thin films were synthesized with comparable parameters that allowed for morphological analysis with scanning electron microscopy of nanoparticle size and shape with respect to deposition thickness and deposition temperature. A trend was noted that confirmed hypotheses of increasing silver cluster density at higher deposition thicknesses and the formation of larger nanoparticle at elevated temperatures. Aluminum depositions were conducted with an aluminum rod and aluminum powder to determine effective source material. Thin films of aluminum were also synthesized with respect to deposition thickness and temperature and analyzed with energy-dispersive X-ray spectroscopy as well as X-ray diffraction. Surface morphology and nanoparticle characterization was conducted with scanning electron microscopy. A trend of increasing nanoparticle size with increasing deposition thickness as well as increasing nanoparticle size with elevated temperatures was observed. Further study in this field will elucidate the surface-enhancement of silver and aluminum tuned with this method.

4.2 Future Plans

Future studies involve further characterization of fabricated thin films as well as investigations with Raman spectroscopy. For a more quantitative understanding of thin film growth and evaporation rate, determination of film thickness is necessary. Additionally, for more precise growth of metal thin films, a quartz crystal thin film monitor can be utilized while depositing. Investigation of a technique for uniform thin film growth with the electron beam evaporation is also necessary to deposit thin films reproducibly. Deposition of aluminum onto quartz substrates for analysis of tuned aluminum nanoparticles with a UV-Vis spectrophotometer would provide further understanding of the absorption peaks for LSPR. Deposition of both Ag and Al onto silicon substrates would allow for ellipsometry analyses. Ultimately, experimentation with Raman spectroscopy would give confirmation of SERS and more information about optimal parameters for maximal enhancement.

APPENDIX

APPENDIX

Instrumentation and Reference Figures

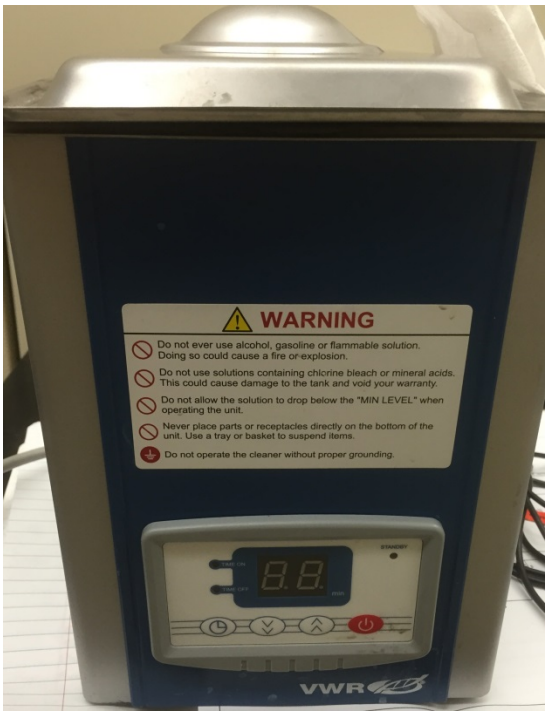

Figure 2.2.1: VWR Ultrasonic Cleaner

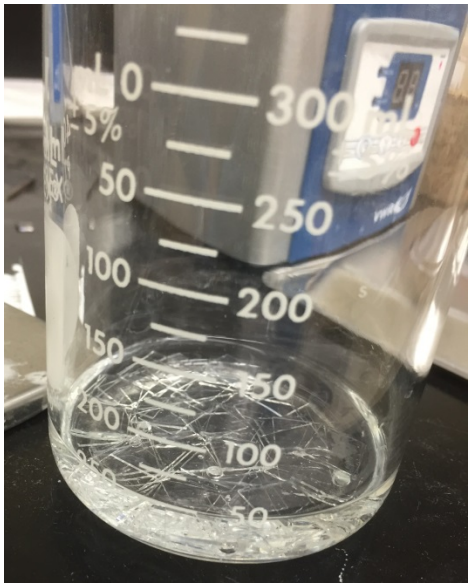

Figure 2.2.2: Partitioned glass slides submerged in ethanol

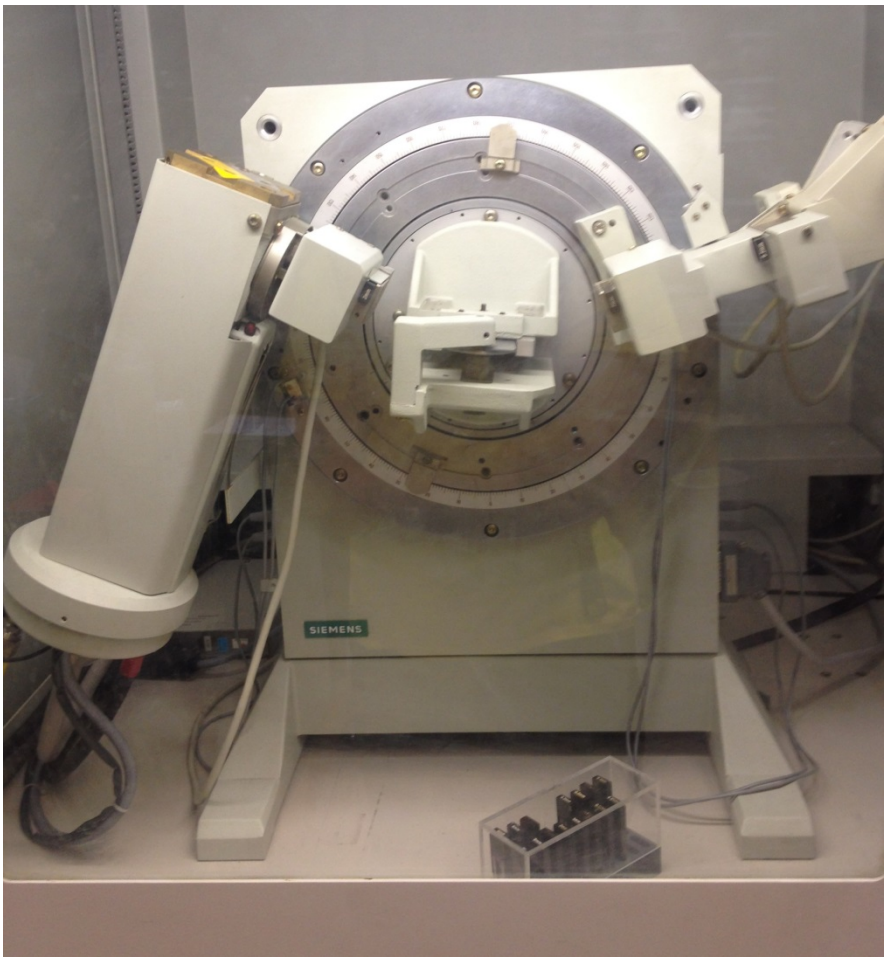

Figure 2.4.1: Siemens D5000 X-Ray Diffractometer

Figure 2.4.2: FEI Versa 3D DualBeam Scanning Electron Microscope

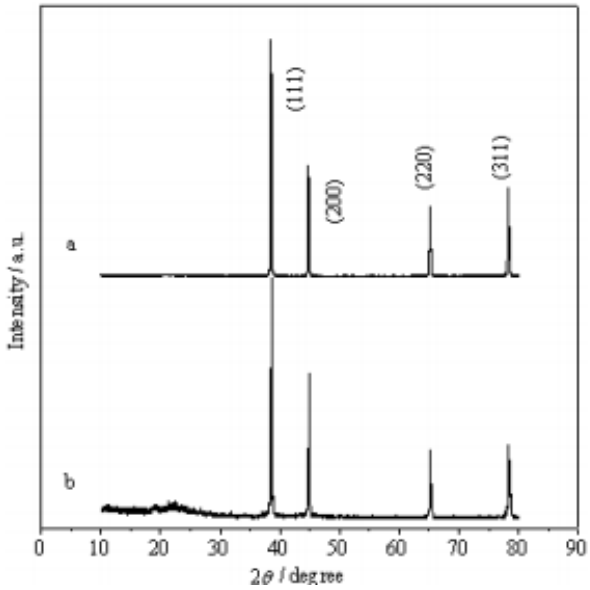

Figure 1: XRD pattern of pure aluminum and aluminum/carbon composite: (a) pure aluminum, (b) composite [26]

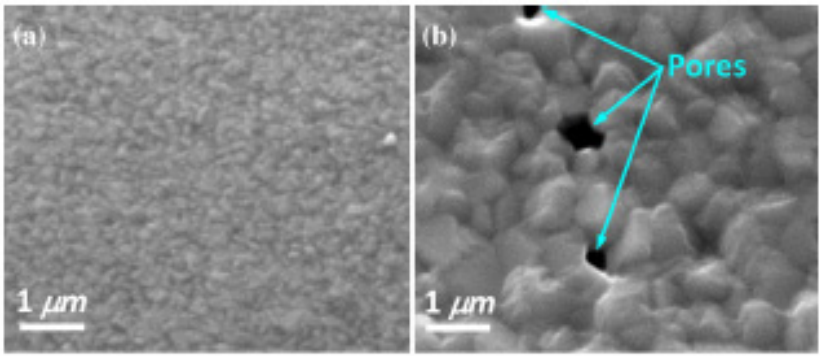

Figure 2: SEM images of (a) RT-deposited aluminum and (b) 150 °C-deposited aluminum [27]

REFERENCES

[1] Raman, C. V., and K. S. Krishnan. “Polarisation of Scattered Light-quanta.”*Nature* 122.3066 (1928): 169. Web.

[2] Vickerman, J. C., and Ian S. Gilmore. “Vibrational Spectroscopy from Surfaces.”Surface Analysis: The Principal Techniques. 2nd ed. Chichester, U.K.: Wiley, 2009. 333-89. Print.

[3] Haynes, Christy L., Adam D. Mcfarland, and Richard P. Van Duyne. "Surface-Enhanced Raman Spectroscopy." *Analytical Chemistry* 77.17 (2005): 338 A-46 A. Web.

[4] Jeanmaire, D. L., and R. P. Van Duyne. "Surface Raman Spectroelectrochemistry Part I. Heterocyclic, Aromatic, and Aliphatic Amines Adsorbed on the Anodized Silver Electrode." *Journal of Electroanalytical Chemistry* 84.1 (1977): 1-20. Web.

[5] Stiles, Paul L., Jon A. Dieringer, Nilam C. Shah, and Richard P. Van Duyne. "Surface-Enhanced Raman Spectroscopy." *Annual Review of Analytical Chemistry* 1.1 (2008): 601-26. Web.

[6] Moskovits, Martin. "Surface-enhanced Raman Spectroscopy: A Brief Retrospective." *Journal of Raman Spectroscopy* 36.6-7 (2005): 485-96. Web.

[7] Kerker, M., D.-S. Wang, and H. Chew. "Surface Enhanced Raman Scattering (SERS) by Molecules Adsorbed at Spherical Particles." *Applied Optics* 19.19 (1980): 3373. Web.

[8] Zhang, Xiaoyu, Matthew A. Young, Olga Lyandres, and Richard P. Van Duyne. "Rapid Detection of an Anthrax Biomarker by Surface-Enhanced Raman Spectroscopy." *Journal of the American Chemical Society* 127.12 (2005): 4484-489. Web.

[9] Haynes, Christy L., Chanda Ranjit Yonzon, Xiaoyu Zhang, and Richard P. Van Duyne. "Surface-enhanced Raman Sensors: Early History and the Development of Sensors for Quantitative Biowarfare Agent and Glucose Detection." *Journal of Raman Spectroscopy* 36.6-7 (2005): 471-84. Web

[10] Grubisha, Desiree S., Robert J. Lipert, Hye-Young Park, Jeremy Driskell, and Marc D. Porter. "Femtomolar Detection of Prostate-Specific Antigen: An Immunoassay Based on Surface-Enhanced Raman Scattering and Immunogold Labels." *Analytical Chemistry* 75.21 (2003): 5936-943. Web.

[11] Lee, Donghoon, Sangyeop Lee, Gi Hun Seong, Jaebum Choo, Eun Kyu Lee, Dae-Gab Gweon, and Sanghoon Lee. "Quantitative Analysis of Methyl Parathion Pesticides in a Polydimethylsiloxane Microfluidic Channel Using Confocal Surface-Enhanced Raman Spectroscopy." *Applied Spectroscopy* 60.4 (2006): 373-77. Web.

[12] Sylvia, James M., James A. Janni, J. D. Klein, and Kevin M. Spencer. "Surface-Enhanced Raman Detection of 2,4-Dinitrotoluene Impurity Vapor as a Marker To Locate Landmines." *Analytical Chemistry* 72.23 (2000): 5834-840. Web.

[13] Ling, X., et al. "Raman Enhancement Effect on Two-Dimensional Layered Materials: Graphene, h-BN and MoS2." *Nano Letters* 14.6 (2014): 3033-40. Web.

[14] Fleischmann, M., P. J. Hendra, and A. J. McQuillan. "Raman Spectra of Pyridine Adsorbed at a Silver Electrode." *Chemical Physics Letters* 26.2 (1974): 163-6. Web.

[15] *Silver Nanoparticle Applications In the Fabrication and Design of Medical and Biosensing Devices*. N.p.: Springer Verlag, 2015. Print.

[16] Park, Hyoung Kun, Jae Keun Yoon, and Kwan Kim. "Novel Fabrication of Ag Thin Film on Glass for Efficient Surface-Enhanced Raman Scattering." *Langmuir* 22.4 (2006): 1626-629. Web.

[17] Lu, Yu, Gang L. Liu, and Luke P. Lee. "High-Density Silver Nanoparticle Film with Temperature-Controllable Interparticle Spacing for a Tunable Surface Enhanced Raman Scattering Substrate." *Nano Letters* 5.1 (2005): 5-9. Web.

[18] Park, Hyoung Kun, Jae Keun Yoon, and Kwan Kim. "Novel Fabrication of Ag Thin Film on Glass for Efficient Surface-Enhanced Raman Scattering." *Langmuir* 22.4 (2006): 1626-629. Web.

[19] Ji, Nan, Weidong Ruan, Chunxu Wang, Zhicheng Lu, and Bing Zhao. "Fabrication of Silver Decorated Anodic Aluminum Oxide Substrate and Its Optical Properties on Surface-Enhanced Raman Scattering and Thin Film Interference." *Langmuir* 25.19 (2009): 11869-1873. Web.

[20] Tian, Zhong-Qun, Bin Ren, and De-Yin Wu. "Surface-Enhanced Raman Scattering: From Noble to Transition Metals and from Rough Surfaces to Ordered Nanostructures." *The Journal of Physical Chemistry B* 106.37 (2002): 9463-483. Web.

[21] Maidecchi, Giulia, Grazia Gonella, Remo Proietti Zaccaria, Riccardo Moroni, Luca Anghinolfi, Angelo Giglia, Stefano Nannarone, Lorenzo Mattera, Hai-Lung Dai, Maurizio Canepa, and Francesco Bisio. "Deep Ultraviolet Plasmon Resonance in Aluminum Nanoparticle Arrays." *ACS Nano* 7.7 (2013): 5834-841. Web.

[22] Chan, George H., Jing Zhao, George C. Schatz, and Richard P. Van Duyne. "Localized Surface Plasmon Resonance Spectroscopy of Triangular Aluminum Nanoparticles." *Journal of Physical Chemistry C* 112.36 (2008): 13958-3963. Web.

[23] Knight, Mark W., Lifei Liu, Yumin Wang, Lisa Brown, Shaunak Mukherjee, Nicholas S. King, Henry O. Everitt, Peter Nordlander, and Naomi J. Halas. "Aluminum Plasmonic Nanoantennas." *Nano Letters* 12.11 (2012): 6000-004. Web.

[24] Taguchi, Atsushi, Yuika Saito, Koichi Watanabe, Song Yijian, and Satoshi Kawata. "Tailoring Plasmon Resonances in the Deep-ultraviolet by Size-tunable Fabrication of Aluminum Nanostructures." *Applied Physics Letters* 101.8 (2012): 081110. Web.

[25] Langhammer, Christoph, Markus Schwind, Bengt Kasemo, and Igor Zorić. "Localized Surface Plasmon Resonances in Aluminum Nanodisks." *Nano Letters* 8.5 (2008): 1461-471. Web.

[26] Lei, Xue-Feng, and Jun-Xian Ma. "Synthesis and Electrochemical Performance of Aluminum Based Composites." *Journal of the Brazilian Chemical Society* 21.2 (2010): 209-13. Web.

[27] Ben-David, E., M. Landa, M. Janovská, H. Seiner, O. Gutman, T. Tepper-Faran, and D. Shilo. "The Effect of Grain and Pore Sizes on the Mechanical Behavior of Thin Al Films Deposited under Different Conditions." *Acta Materialia* 87 (2015): 321-31. Web.